S-wave anisotropy from two dipole sonic data processing methods, confronted with fracture permeability, logs and cores

José Perrin, Didier Belaud, Jean-Pierre Yver, Charles Naville

Science and Technology for Energy Transition **77**, 13 (2022)

https://doi.org/10.2516/stet/2022006

Available online at:
stet-review.org

REVIEW ARTICLE OPEN ACCESS

S-wave anisotropy from two dipole sonic data processing methods, confronted with fracture permeability, logs and cores

José Perrin[1,a], Didier Belaud[2,a], Jean-Pierre Yver[2,a], and Charles Naville[3,*]

[1] BRGM, 3 Claude Guillemin BP 36009, 45060 Orléans Cedex 02, France
[2] Services Petroliers Schlumberger, 42 rue St Dominique, 75007 Paris, France
[3] IFPEN, 1 et 4, Avenue de Bois-Preau – BP 311, 92852 Rueil Malmaison Cedex, France

Received: 18 October 2021 / Accepted: 25 March 2022

Abstract. The present paper consists in two parts, determined by the historical emerging production of Dipole Sonic Imager (DSI[1]) measurements and results in the early 1990's. The DSI data were processed following two methods simultaneously developed in France and in USA by *Schlumberger*. In the first part the early dipole sonic S-wave velocity results obtained in late 1993 are confronted with the other borehole data obtained in the scientific borehole MM-1, entirely cored and extensively logged, as part of the comprehensive scientific project named Géologie Profonde de la France (GPF), conducted by the *Bureau de Recherches Géologiques et Minières* (*BRGM*, *i.e.* the French Geological Survey), in Ardèche, southern France. In 1994, José Perrin summarized and integrated all the borehole information including the preliminary results from an azimuthal "rotation scan" of S-wave sonic slowness determination method quickly developed in *Schlumberger-France* and aiming at detecting only the presence of S-wave velocity anisotropy in a first step. The initial results were presented to the French industrial logging community in April 1994, prior to the commercialization of any S-wave splitting computer detection routine applied to dipole sonic data. The second part focuses on the comparison of the dipole sonic S-wave anisotropy detection results from two methods produced at a later time by *Schlumberger*, namely: a) results from the commercial S-wave anisotropy detection routine based on cross energy minimization, obtained in October 1994, and b) principal S-wave azimuth results sorted from the "rotation scan" azimuthal method, produced in 1995 and further improved in July 1997. After discussing the discrepancies of the principal fast S-wave azimuth derived from the two methods with diverse specialists in *Schlumberger*, over several years, and on a spare time basis, the authors expose constructive explanations in the present paper. A limited overview of the latest dipole sonic data processing developments has also been attempted to better understand the differing S-wave birefringence results obtained in MM-1, suggesting that the rock formation in the immediate borehole vicinity, up to three times the borehole radius, may not be homogeneous along the borehole depth depending on the local geological context. Besides, the Fast Azimuth split S-wave (FAZ) fits with the strike of major regional faults and parallel to the maximal horizontal palaeo-stress, which happens to be nearly orthogonal to the local present stress direction accepted by the geologists! The present case study suggests that the S-wave anisotropy results ought to become more reliable, mainly on the accuracy and precision of the FAZ. Additionally, the efficiency of the semblance parameter for S-wave attenuation anisotropy detection is pondered, where no S-wave velocity anisotropy is detected over the dipole sonic receiver array.

Keywords: Shear wave, SWS, Shear wave splitting, Birefringence, Acoustical birefringence, Dipole sonic, Borehole sonic, Flexural shear wave, Anisotropy, Stress, Fracture, Permeability, Cores, STC, Slowness time coherence.

* Corresponding author: Charles.naville@ifpen.fr

[a] Retired.

[1] Trademark of *Schlumberger*.

1 Introduction

Dipole sonic logging tools have been used by geomechanical drilling/completion engineers in the late 1980's in the aim to obtain Shear wave velocity information, thus Young modulus information, in the weakly compacted, low velocity shallow terrains located right below seabed. Knowledge of the Shear modulus at shallow drilling depths helps evaluating the borehole wall stability issues and setting the conductor casing and shallow casing points. As a matter of fact, when the S-wave velocity of the borehole wall rocks is lower than the mud velocity, or Stoneley/tube wave velocity, the sonic S-wave arrival generated by a sonic monopole pressure source in the fluid filled borehole is not refracted any more along the borehole wall and does not exist anymore. Therefore, borehole dipole sonic tools were designed and implemented in order to generate flexural shear wave propagated as direct S-waves along the borehole wall, and generating volume S-wave into the rock formation allowing the possibility to record S-wave reflected away from the borehole back onto the dipole sonic shear wave receivers, for any industrial application.

Around 1990, when the initial borehole dipole sonic tools were built, the orientation issue of dipole transmitters and dipole receivers naturally arose, and was addressed by the dipole sonic manufacturers by mounting TWO orthogonal transmitters and TWO orthogonal receivers at each receiver position, in the plane orthogonal to the tool axis, in order to record all kinds of S-wave signals, in all possible azimuths. Consequently, an orientation measurement tool was combined with the wireline dipole sonic tool, thus becoming fully appropriate for acoustical polarimetric measurements along the well axis, in the main sonic wave propagation direction.

The first part of the present paper relates to the material and data collected in 1993 in the 1000 m deep MM-1 coredrill, undertaken by *BRGM* as part of the Géologie Profonde de la France (GPF) scientific project, described by Bonijoly *et al.* [1]. The collected borehole data comprises a whole set of common logs recorded while drilling, and wireline logs. The diversity of the acquired measurements allows to observe the expression of the same phenomena with redundancy, and to compare the responses from different methods. Detecting permeable fractures and permeable depth levels was derived from a variety of applied methods: geochemical monitoring of the drilling fluid returned to surface, resistivity logs, fluid temperature logs recorded months after drilling, Formation Resistivity MicroScanner (FMS, see Footnote 1) images of the borehole wall, azimuthal Shear wave Dipole Sonic Imager (DSI) response, all the above being crosschecked by observations on cores. All the borehole information including the dipole sonic results processed by *Schlumberger-France* and summarized by J. Perrin in 1994 have been presented on April 6, 1994 at the SAID Technical Meeting in Paris, France (SAID stands for "*Société pour l'Avancement et l'Interprétation des Diagraphies*"/the French branch of *SPWLA*), but were left unpublished until now.

The second part focuses on the technical comparison of additional dipole sonic S-wave anisotropy detection results from two distinct methods implemented by *Schlumberger*, namely: a) results from the commercial S-wave anisotropy detection routine based on cross energy minimization, issued in October 1994, and b) sorted principal S-wave azimuth results from the "rotation scan" azimuthal method, produced in 1995 and further improved in July 1997.

The discrepancies of the principal fast S-wave azimuth observed from the two methods were discussed with diverse specialists in *Schlumberger*, over several years, and on a spare time basis: the authors expose constructive explanations for these discordance between results, which calls for additional data analysis.

The latest dipole sonic data processing methods developed by the dipole sonic industry has also been overviewed in order to improve our understanding of the differing S-wave birefringence results obtained in MM-1.

Despite the apparent contradictory birefringence results obtained in the Ardèche MM-1 coredrill are still felt sufficiently innovative and perplexing by the authors to justify an extended publication.

2 GPF project motivation and geological context (1991–1993)

2.1 GPF-Ardèche project overview

The main objective of the GPF project was to characterize and quantify the rock mass transfers associated with the structuration process of the distensive paleomargin of the Ardèche area. The studied site is located 12 km south of Aubenas (Fig. 1), it had been retained because of its immediate vicinity with the mineral district of Largentière, where numerous, well-known paleo fluid flow hints are present.

Therefore, locating and characterizing the permeable zones in the planned boreholes constitute an essential part of this project.

2.2 Structural context, paleo-stress

In 1989, a geophysical campaign of field measurements including 2D seismic and gravimetry was conducted to complement the existing structural sketch of the studied area (Fig. 2).

In particular, the newly acquired seismic sections fully processed using depth migration, revealed an important normal faulting system of Jurassic age, or poorly expressed from the outcrop, namely the Balazuc fault and Uzer fault (Fig. 3). These main elongated faults oriented along the N30E–N40E Cevenole trend, are intersected by accidents locally transverse to the margin. They probably represent the initial manifestation of the Ardèche margin evolution between the continent and the South–East basin, and probably played a leading role on the fluid circulation during the diagenesis.

In order to confirm the fault influence on fluid flows, two scientific wells, located 1200 m apart, along the northern seismic profile, were drilled in the aim to core the Liassic and Triassic reservoirs (BA-1 and MM-1, respectively drilled in 1991 and 1993). These two wells confirmed the

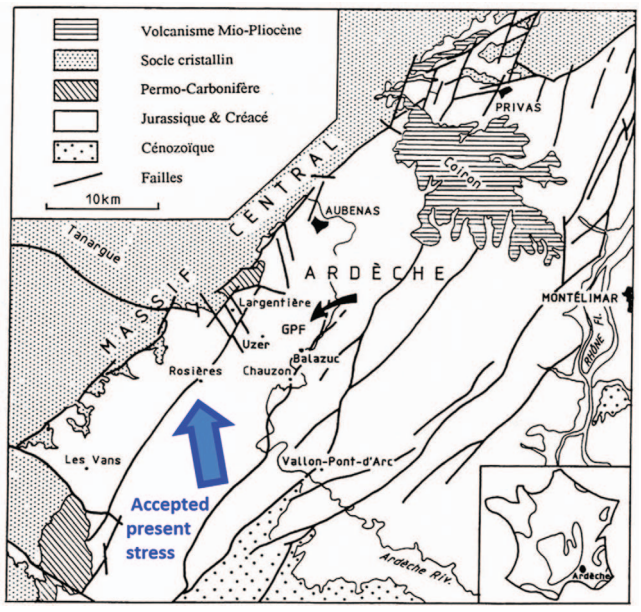

Fig. 1. GPF-Ardèche project: geological sketch and site location in SE France.

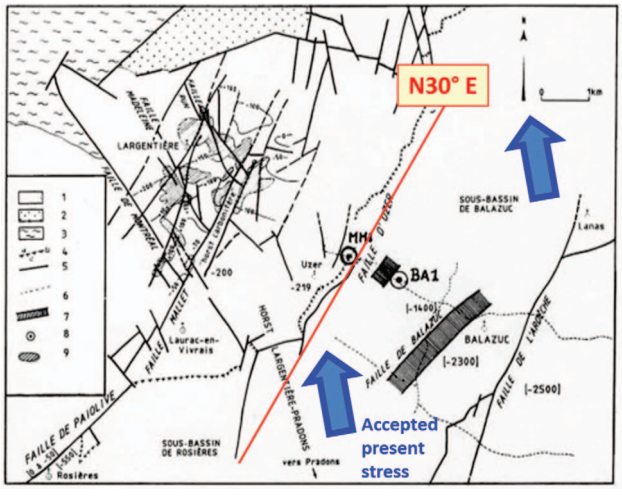

Fig. 2. GPF-Ardèche project: Structural sketch, modified from *Fig.1 of Giot et al.* [3]. Legend: (1) Mesozoic sedimentary cover, (2) Permian, (3) Basement, (4) Paleosurface with thin sedimentary deposits, (5) visible faults, (6) seismic lines/GPF project, (7) Faults revealed by seismic, (8) GPF boreholes BA-1 and MM-1, (9) Largentière sulfur deposits.

existence of the major Uzer fault, 1300 m throw, and refines its geometry (Fig. 4). Extensive details of this newly discovered fault are expressed by Giot *et al.* [2], enlightening the dynamics of the local Jurassic passive margin (Giot *et al.* [3]). All the GPF program results were later integrated in the context of the Mesozoic evolution of a part of the Tethyan continental margin, by Bonijoly *et al.* [4].

Interestingly, the S-wave birefringence response from the MM-1 dipole sonic measurements can be confronted with a detailed study of the paleo stress *versus* depth and geological formation carried out by Martin and Bergerat [5] in the deep Balazuc BA-1 well, in the hanging wall compartment of the Uzer fault. The formations encountered in the MM-1 coredrill are of Hettangian age, Lias to mid-Trias, while the local Mesozoic extension regime was in the NW–SE direction, at right angle to the N30°E strike of the major faults (Figs. 2–4).

2.3 The MM-1 core drill

The MM-1 well was positioned on the upper compartment of the margin and was cored down to 980.35 m. It went through the layers of Hettangian, Trias, Permian, and penetrated the carboniferous terrains (excerpt on Fig. 5). This core drill has been achieved under *BRGM* project management.

The MM-1 well was extensively surveyed, in a manner similar to what was done in the previous BA-1 well, in order to produce a good geological correlation tie between the two wells, as follows:

- Detailed sedimentologic and structural description of the core samples after determination of core orientation.
- Outside surface photography of all core samples by 1 m long sections with a core scan technique.
- Continuous measurements of gamma-density along the cores.
- Hydro-geochemical monitoring of the returned drilling fluids: chemical analysis on mud filtrate and gas analysis, geared at detecting the interstitial fluids and occluded gases trapped inside the rock formation under drilling.
- Comprehensive set of wireline logs, performed by *Schlumberger*; a full set of logs (AMS, NGS, DLL, LDT, CNL, DSI, FMS, acronyms defined at the end of paper) was acquired ONLY in the 0–320 m well phase-I, because the coring HQ diameter (101.6 mm) needed to be enlarged to 6″1/4 (158.8 mm) in order to provide a safe clearance for the wireline logging tools.
- A downhole seismic source experiment with explosives was conducted by *IFP* and *CGG* in order to field test the method of reverse seismic walkaway, using both standard solid explosives as well as liquid, catalyzed explosives, the latter ones facing easier transportation regulations.
- In 1993, all the above data had not been fully analyzed, but were judged very promising from the preliminary interpretations.

2.4 Detection of permeable fractures in the Hettangian

The Hettangian formation (9.45–134.41 m) consists in nodular marl-limestones interbedded with massive dolomitic limestones or sedimentary brecciated limestones layers. They correspond to transgressive lagoon-marine deposits.

In MM-1, the Hettangian limestones exhibit high velocity values (V_p velocity about 4300 m/s).

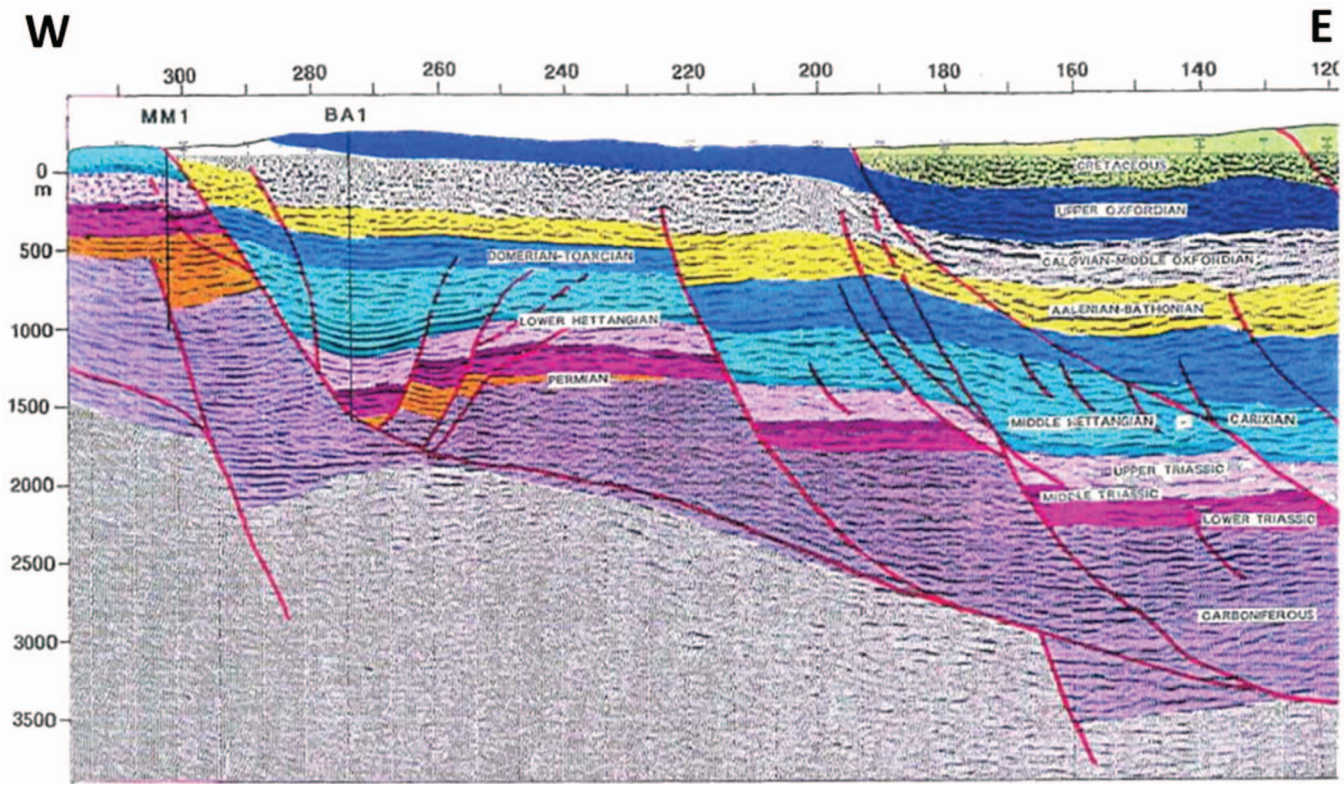

Fig. 3. GPF-Ardèche project: WE structural section MM1 – BA1 from the northern 2D profile, post stack depth migration, true amplitude display. Velocities and reflectors are tied on wells MM-1 and BA-1. Seismic processing by *CGG-France*, Section interpreted by D. Bonijoly-BRGM and the GPF team.

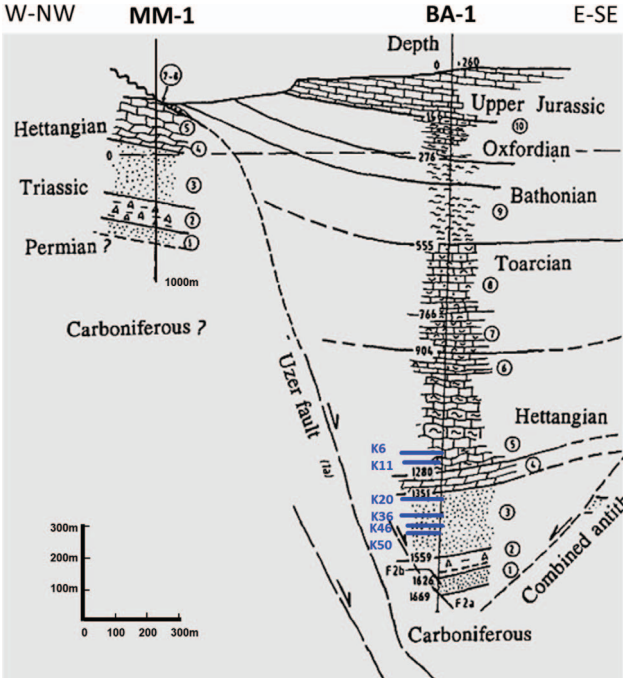

Fig. 4. GPF-Ardèche project: Structural sketch MM1 – BA1, modified from *Figure 1 of Deflandre and Sarda [35]*. K6–K50 are the core positions of Anelastic Strain Measurements (ASR), to be confronted with palaeo stress derived from visual core description (*Martin and Bergerat [5]*), and with FMS borehole wall images.

Several zones of water inflow have been identified by physico–chemical analysis of the fluids returned to surface while drilling: pH, Conductivity, Calcium and Chloride content, clearly appearing at depths: 58, 70, 75, 85 and 93 m (Fig. 6). The depth levels of water flow are evidenced by an increase of salinity and lower pH in the returned drilling fluid. Their depth position is not very precise due to the detection mode operated here: the fluid sampling is loose (3.6 m depth step), and it is not easy to distinguish several inflows located closely in depth, from a repeated fracture inflow from a single depth (70 and 75 m for instance?).

Monitoring the gas kicks in the returned drilling fluid (Fig. 7) also indicates an inflow of Helium and Radon gases while drilling permeable and fluid filled fractured zones (depth levels: 58, 64, 70, 94 m).

The observation of a weak artesian flow during the drilling operation (10 L/mn estimated flow) indicated the depth positions 58 m and 70 m as producing levels.

The Auxiliary Measurement Sonde/AMS logs (Fig. 8) confirm the above fluid flows by significantly perturbed Temperature measurements down to 100 m, marked by two *sharp temperature and conductivity drops at* 54 and 87 m, *bottom to top*. For a correct interpretation of these log results, it is important to take in account their recording conditions:

– Artesian flow occurred at surface after stopping the drilling fluid circulation for 4 h only.

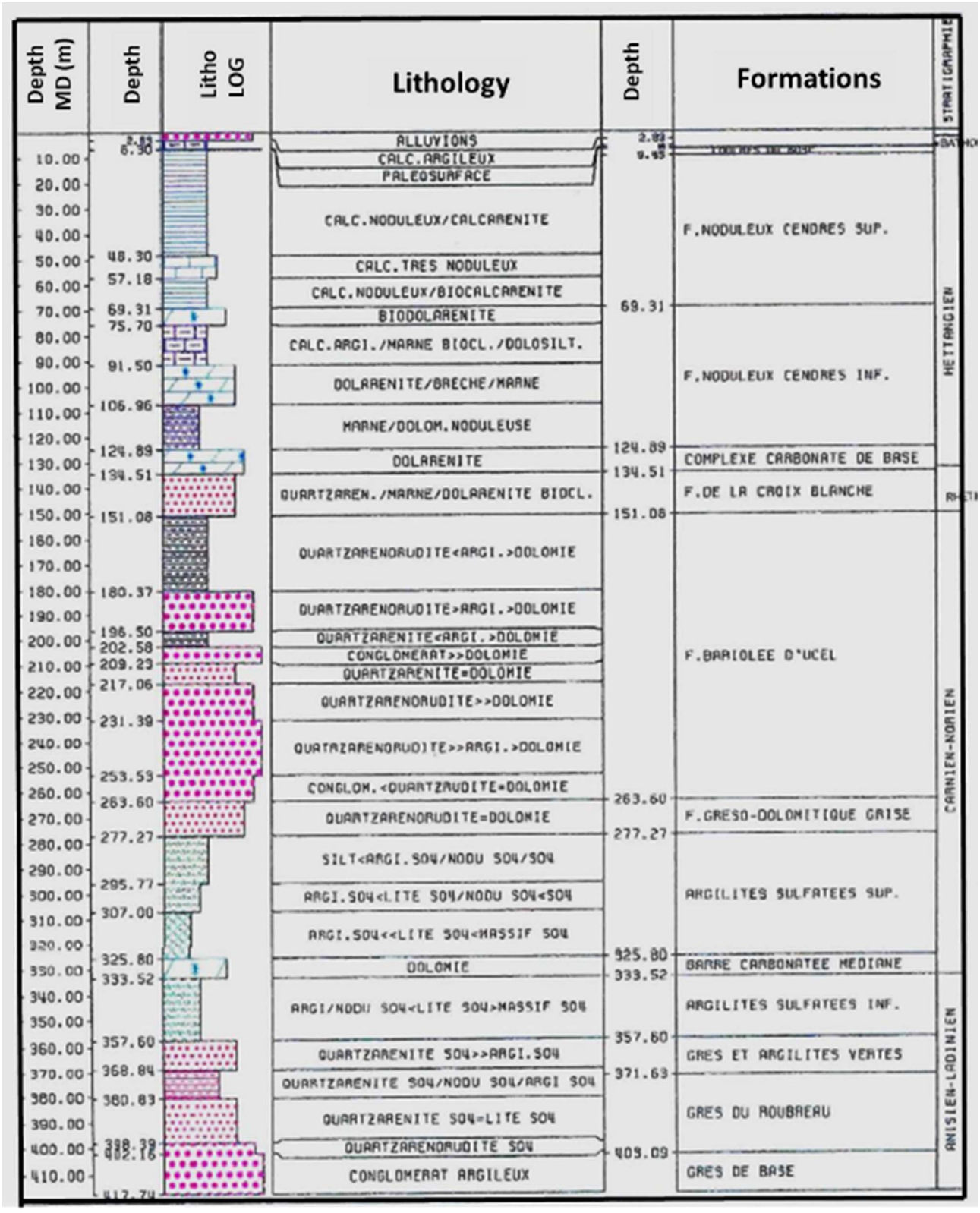

Fig. 5. GPF-Ardèche, MM1 borehole, lithology of Mesozoic, Bathonian to Trias.

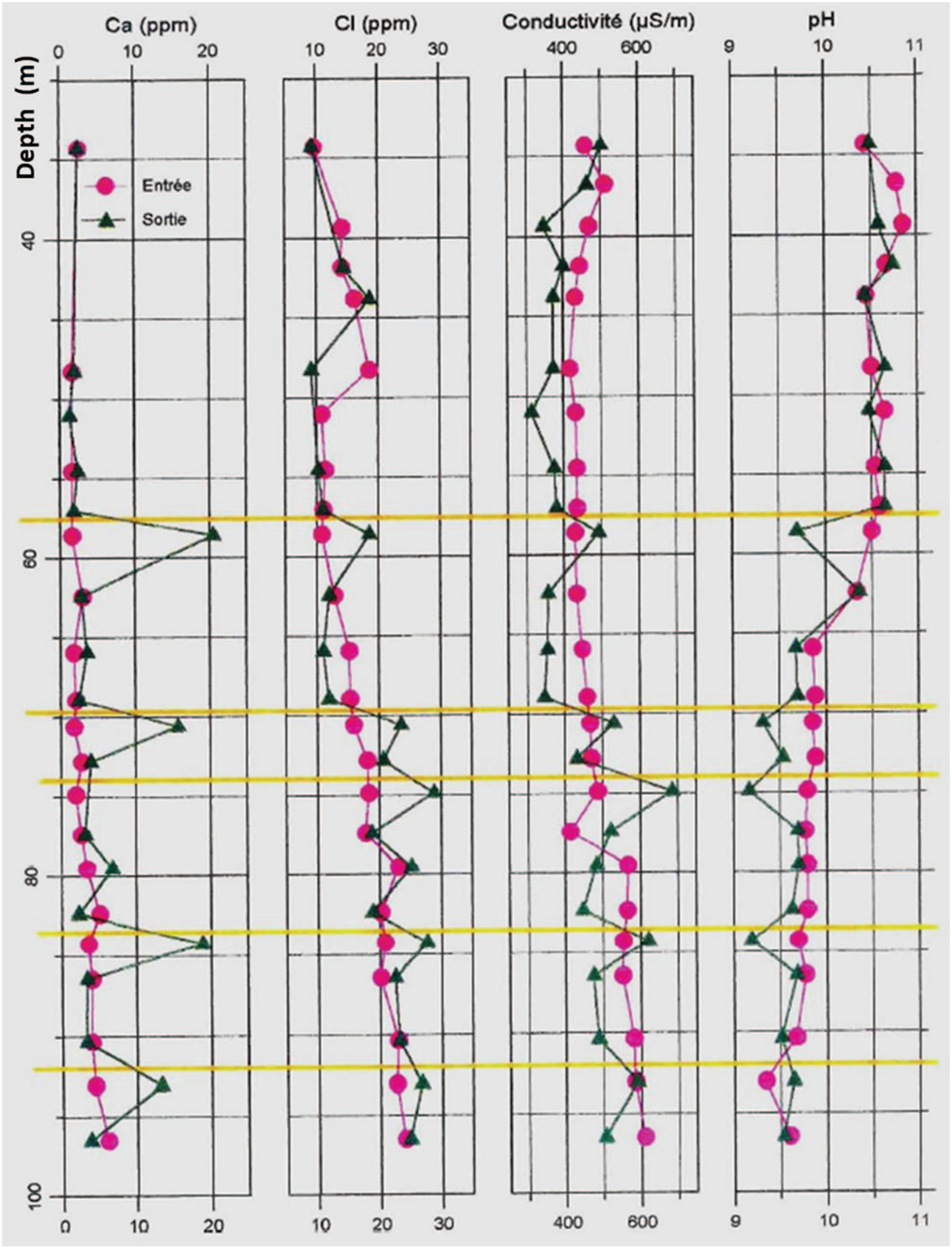

Fig. 6. GPF-Ardèche, MM1 borehole, geochemical results from Mud logging while drilling. The yellow bars indicate depths of confirmed permeability.

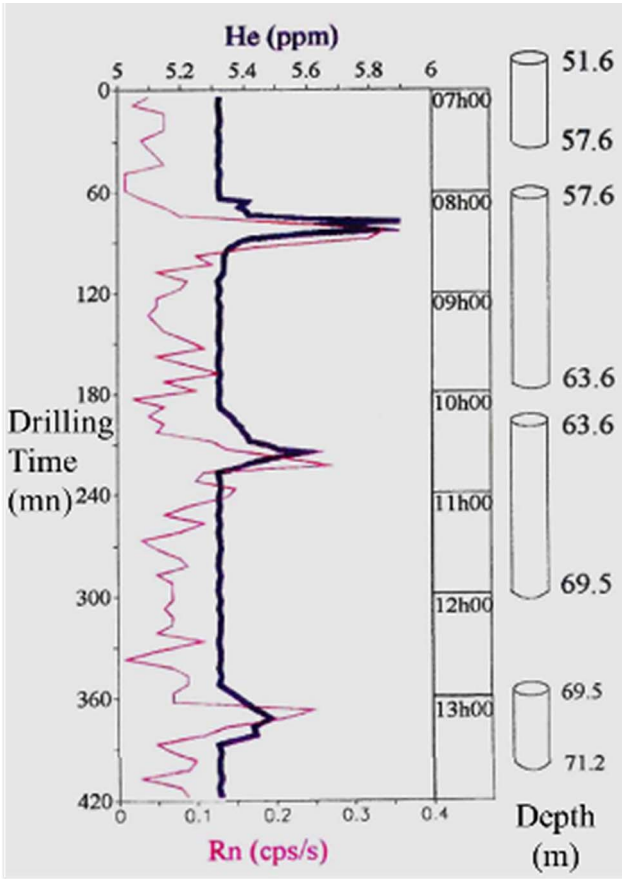

Fig. 7. GPF-Ardèche, MM1 borehole, observations from Gas logging while drilling.

– In contrast with the fluid flow monitoring while drilling, the artesian inflows are marked on logs by decreasing steps of conductivity (bottom *to top*), due to the high salinity of the whole mud column after drilling the sulfated argillites below 277 m. The highest artesian inflow seems to originate from depth level 54 m, with a very homogeneous fluid column above it.

The Spontaneous Potential (SP) log (Track 4 on Fig. 8) complements the previous measurements by exhibiting three negative troughs: 70, 94, 99 m associated with pyrite, well identified on cores at the depth of fractures. Tiny positive peaks at 87 m, and possibly at 54 m could indicate water flows.

The Shear wave splitting propagation in anisotropic medium, or S-wave birefringence, is summarized on the sketch of vertical propagation of Figure 9, where the linear pulse generated by the dipole source in the lower position moves upwards and splits in two orthogonal principal S-waves of different velocities and attenuation while propagating through the anisotropic medium materialized by vertical plane streaks associated with a horizontal axisymmetric axis.

Three attributes characterize the S-wave birefringence:

1. *Azimuth of the fast S-wave principal mode* (the slow S-wave azimuth being orthogonal to the latter).
2. *Anisotropy of Velocity (V), or of slowness (1/V),* preferably measured over the dipole sonic receiver array: $\Delta V/V = 2\ \mathrm{ABS}\ (V2 - V1)/(V1 + V2)$, in percent.
3. *Anisotropy of attenuation, or Differential attenuation* between the two principal S-wave modes propagated along the same geometric ray path, preferably measured over the dipole sonic receiver array.

The three above attributes are usually computed and output from S-wave surface seismic studies and VSP's (Gratacos *et al.* [6]) and Vertical Seismic Profiles (VSP's), although the differential attenuation is often neglected by S-wave explorationists. The S-wave birefringence behavior described for seismic body waves for surface seismic and VSP's (Naville [7]), equally applies to flexural sonic S-waves, both in their low frequency spectrum domain and in their dispersive high frequency spectrum segment.

The interpretation of fractures is a multiscale/multidomain exercise, as reported by Far *et al.* [8], the accurate S-wave birefringence data analysis appears to geoscientists as a very promising tool to characterize the azimuthal anisotropy of fractured rocks under stress at all scales.

Therefore, in August 1993, the DSI dipole sonic tool was run in the scientific MM-1 borehole by *Schlumberger* on an experimental basis, in BCR acquisition mode: the DSI results produced in late 1993-early 1994 derived from a method of Azimuthal S-wave slowness measurement Scan (Rotation-Scan), and only the fast and slow principal S-wave slowness $(1/V)$ logs were produced, as displayed on Figures 10a–10c. Indeed, the DSI results from Rotation-Scan show highly contrasted responses right at the depth levels where water flows from fractures were previously identified on logs and cores.

The S-wave velocity anisotropy appears as a percentage on the solid black $\Delta V/V$ curves on Figures 10a–10c, left side of Track 2, which clearly pinpoint the permeable fractured levels (54, 69–72, 87, 94 m, 202–206 m, 217 m) by S-wave velocity anisotropy peak values up and above 20% (reaching 30% at 94 m).

Figures 10a–10c exhibit, left to right:

– Track 1: max/min C1/C2 diameters from 4 arm Caliper, in red, and Gamma Ray/GR: small and localized ovalisation is present in the cored MM-1 borehole: the hole was enlarged to 6″1/4 before running the DSI tool.
– Track 2: slownesses 40–240 μs/m scale: DTCO, DTSmin (red) and DTSmax (Black) from Rotation-Scan, DTS from monopole transmitter (blue), DTST/Stoneley (black, smooth curve), superimposed with the velocity anisotropy $\Delta V/V$ curve (black, high frequency).
– Tracks 3–5: Lithological columns.

At the permeable depth levels previously detected, the borehole wall images produced by the FMS tool reveal clear open fractures, well identified on the cores and on the core peripheral photographs (Fig. 11), where the 54.8 m deep fracture is associated with a 23% peak anisotropy value (Fig. 10a). The permeable and highly anisotropic 69.5–71.5 m interval (Fig. 10a) corresponds to a fully fractured core (Fig. 12).

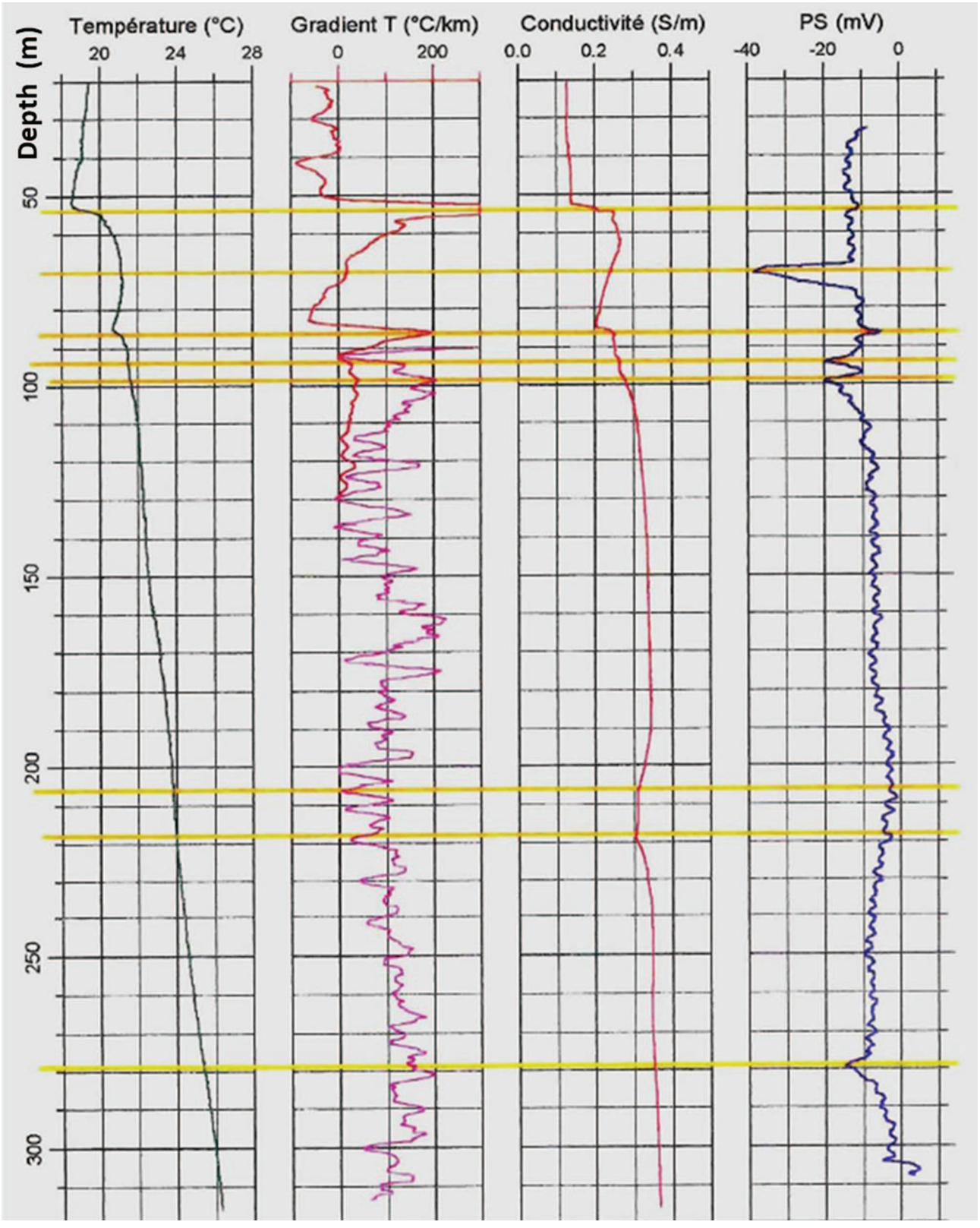

Fig. 8. GPF-Ardèche, MM1 borehole, Wireline logs, in Measured Depth. Left to right: Celsius Temperature (Black), temperature gradient (magenta), Conductivity (red), SP (purple). The yellow bars underline the permeable depth levels of inflow or outflow.

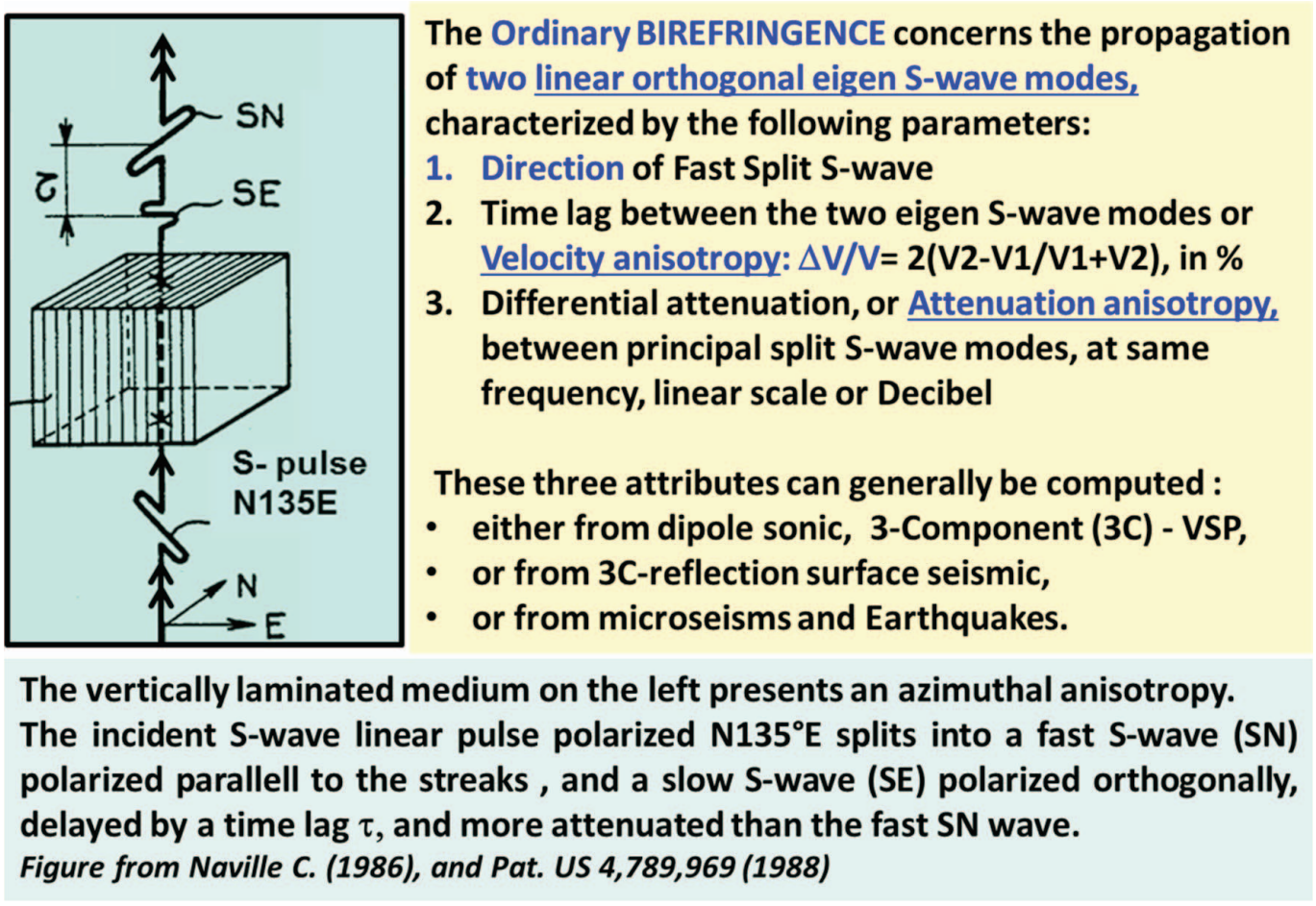

Fig. 9. Illustration of the S-wave birefringence seismic propagation, or Shear-wave Splitting.

In contrast, the tight, closed fractures visible in the 121–126 m interval (Fig. 13) do not exhibit any velocity anisotropy higher than the 7–10% rock matrix velocity anisotropy (Fig. 10b). The tight fractures in this interval are not singled out by the DSI S-wave anisotropy results, meaning that the S-wave anisotropy detection from dipole sonic measurement may potentially help discriminate between open and tight fractures, thus simplifying the task of interpreters and reservoir engineers in their search for permeable fractures.

***Remark*:** The blue curve on Figures 10a–10c/Track 2 represents the DTS/S-wave slowness output result of the standard STC (Slowness-Time-Coherence) routine applied to the monopole DSI measurements; the standard monopole STC processing also provided the P-wave slowness (DTCO) and the Stoneley slowness (DTST) curves, presented on the same Figures 10a–10c. The monopole DTS slowness is expectedly intermediate between the DTSmin and DTSmax slownesses of the principal S-wave modes determined by the rotation scan method, at most of the depths; however, in specific depth intervals, the monopole DTS slowness is much closer either to the DTSmin or to the DTSmax slowness values output from the Rotation-scan. We have no explanation for this result, except that the flexural S-wave mode is different between monopole and dipole propagations, the S-wave frequency content might be different between the monopole and the dipole emitters, with a different dispersive wave segment on the flexural S-wave spectrum, and possibly with different attenuation *versus* frequency relationships of the considered S-wave modes. The "hastily" processing applied in the early 1990's on the early DSI dataset of MM-1 could not take in account any dispersive characteristics of the flexural S-wave modes, mostly unknown at the time.

Figure 14 exhibits the FMS images of the highly permeable and anisotropic 87 and 94 m fractured brecciated levels (Track 3), with gamma ray (green curve on Track 2), associated with the dipmeter results, expressing a constant 5° downdip towards N30°W (Track 1).

Therefore, we will consider that the geological layering or bedding is near horizontal, and that the MM-1 borehole is vertical, with negligible hole ovality in the shallow 300 m below Ground level. Although the apparent SE downdip in the shallow 80 m from the seismic section on Figures 3 and

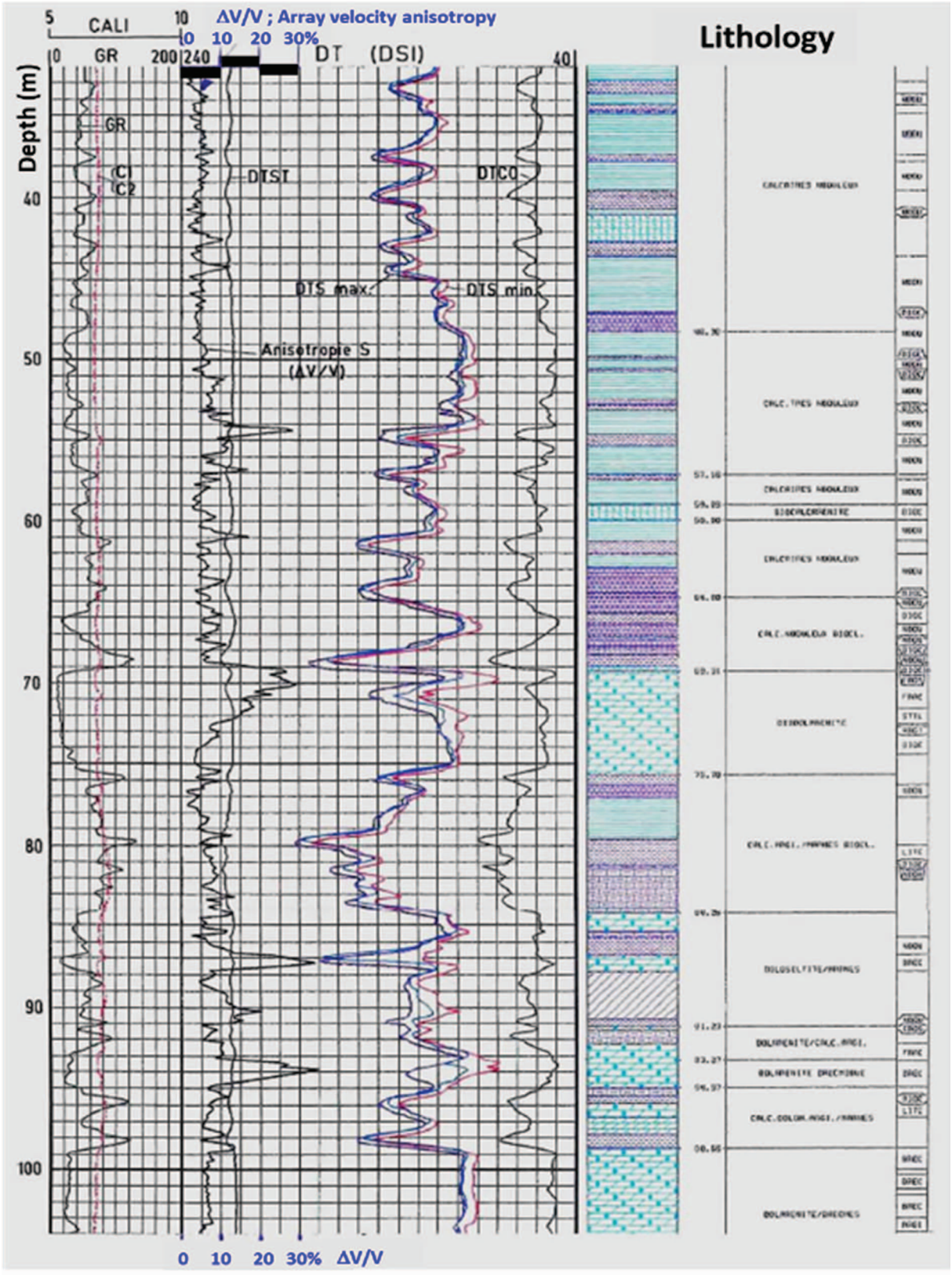

Fig. 10a. MM1 borehole, 32–104 m, S-wave velocity anisotropy results from Rotation-scan. Track 1: max/min C1/C2 diameters from 4 arm Caliper, in red, and Gamma Ray/GR. Track 2: slownesses 40–240 μs/m: DTCO, DTSmin (red) and DTSmax (Black) from Rotation-Scan, DTS from monopole transmitter (blue), DTST/Stoneley (black, smooth curve), superimposed with the velocity anisotropy $\Delta V/V$ curve (black, high frequency). Tracks 3–5: Lithological columns.

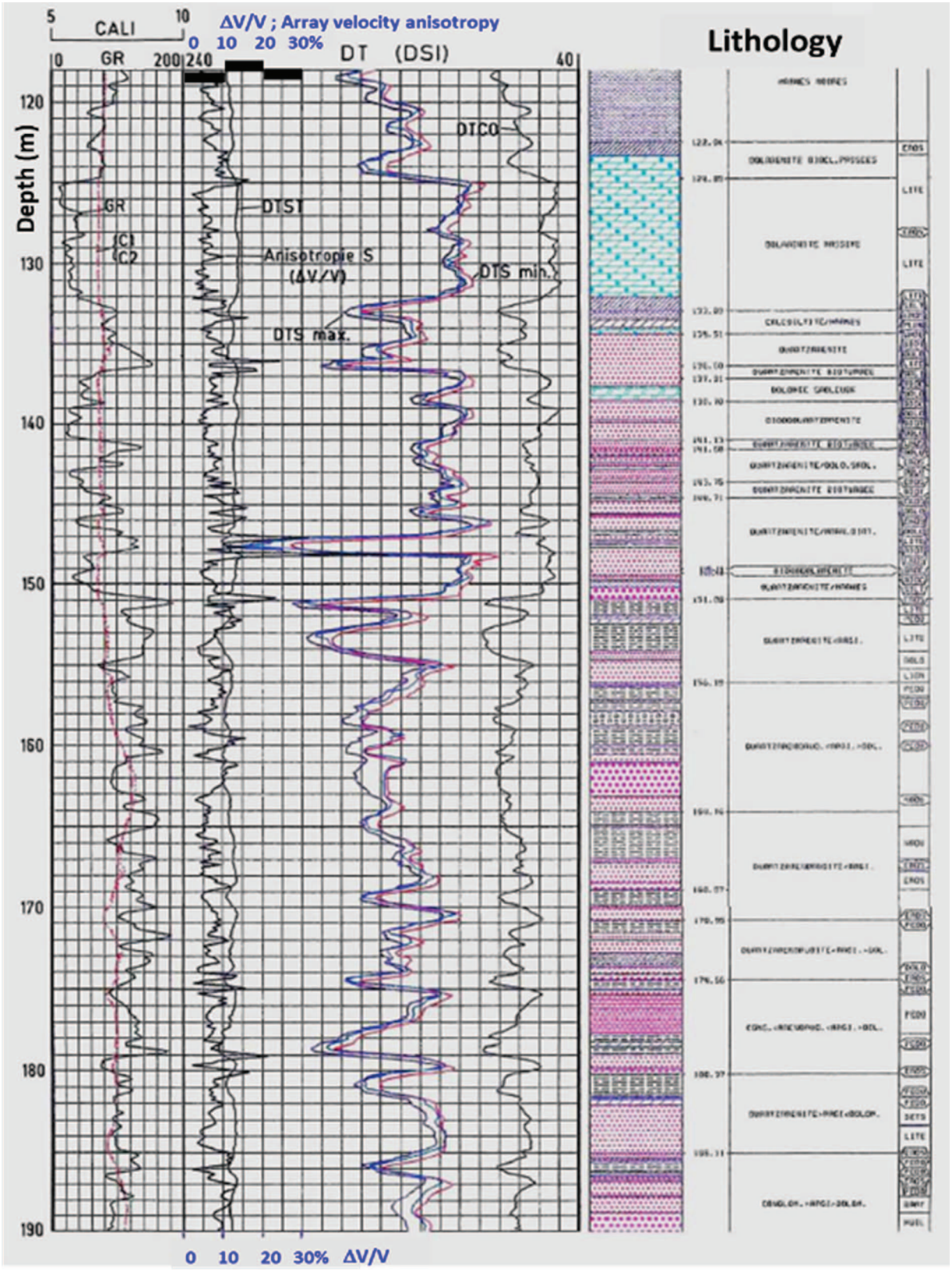

Fig. 10b. MM1 borehole, 118–190 m, S-wave velocity anisotropy results from Rotation-scan. Track 1: max/min C1/C2 diameters from 4 arm Caliper, in red, and Gamma Ray/GR. Track 2: slownesses 40–240 μs/m: DTCO, DTSmin (red) and DTSmax (Black) from Rotation-Scan, DTS from monopole transmitter (blue), DTST/Stoneley (black, smooth curve), superimposed with the velocity anisotropy $\Delta V/V$ curve (black, high frequency). Tracks 3–5: Lithological columns.

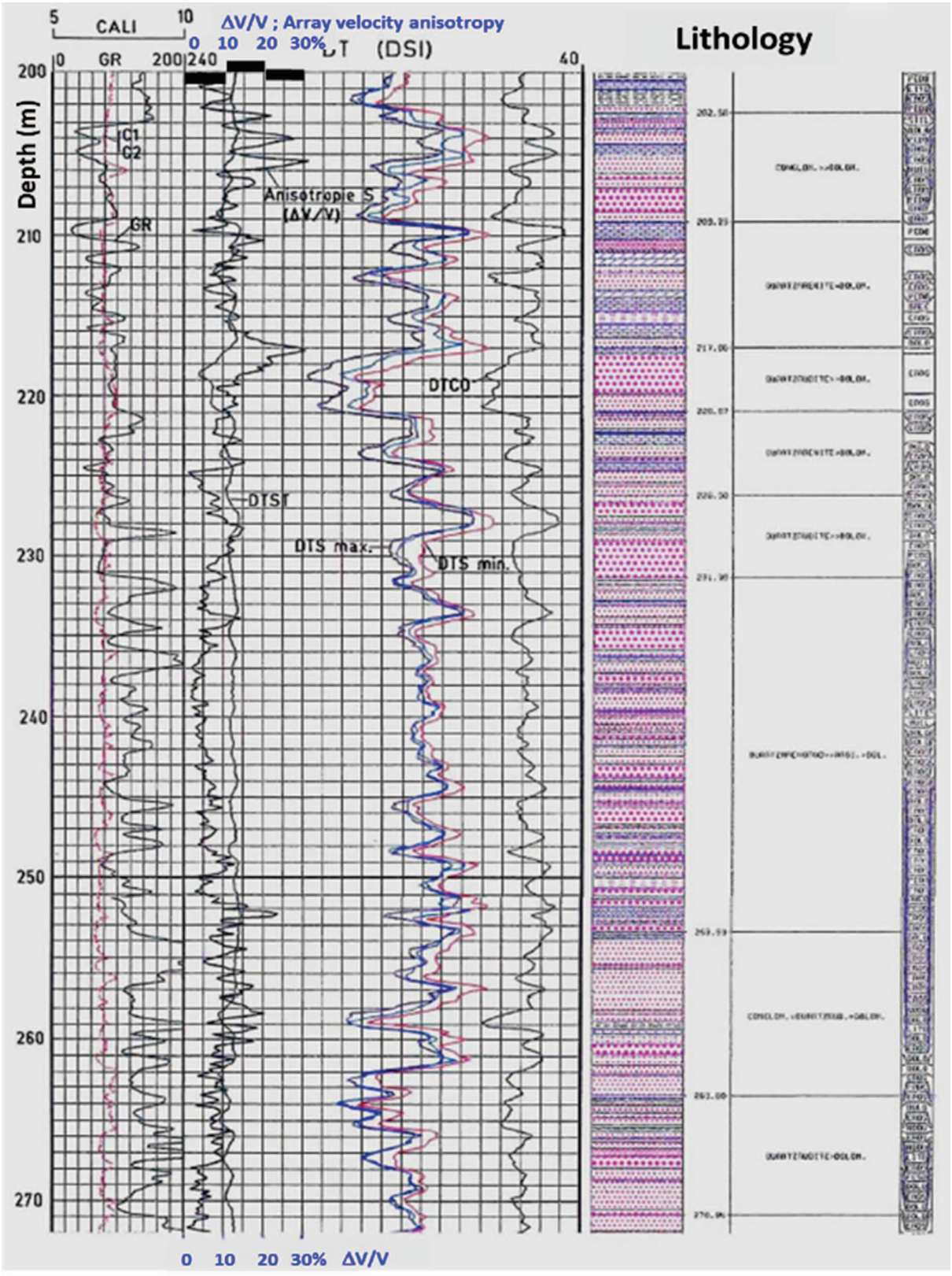

Fig. 10c. MM1 borehole, 200–272 m, S-wave velocity anisotropy results from Rotation-scan. Track 1: max/min C1/C2 diameters from 4 arm Caliper, in red, and Gamma Ray/GR. Track 2: slownesses 40–240 μs/m: DTCO, DTSmin (red) and DTSmax (Black) from Rotation-Scan, DTS from monopole transmitter (blue), DTST/Stoneley (black, smooth curve), superimposed with the velocity anisotropy $\Delta V/V$ curve (black, high frequency). Tracks 3–5: Lithological columns.

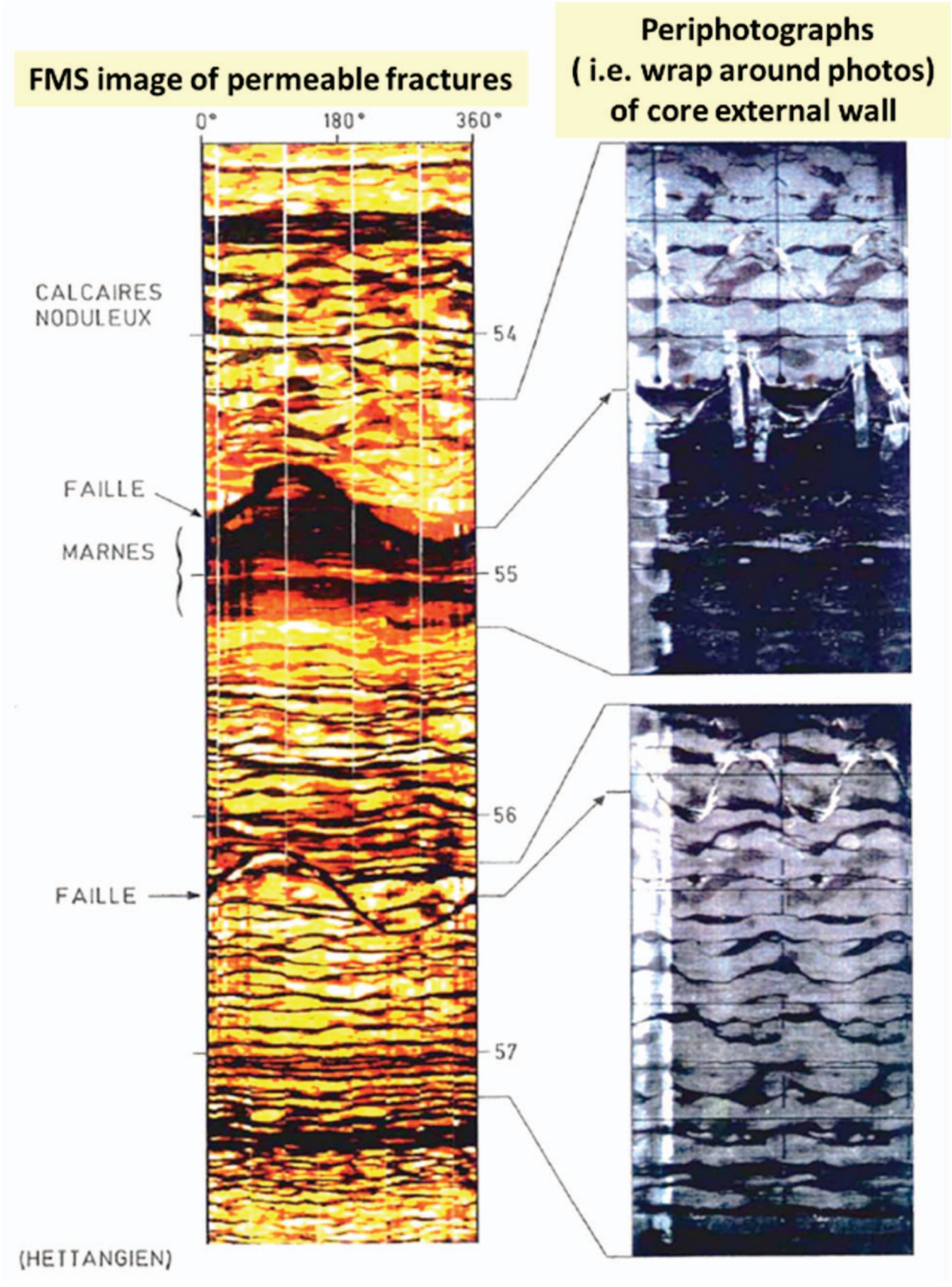

Fig. 11. GPF-Ardèche, MM1 borehole wall images and core periphotographs, 53–58 m.

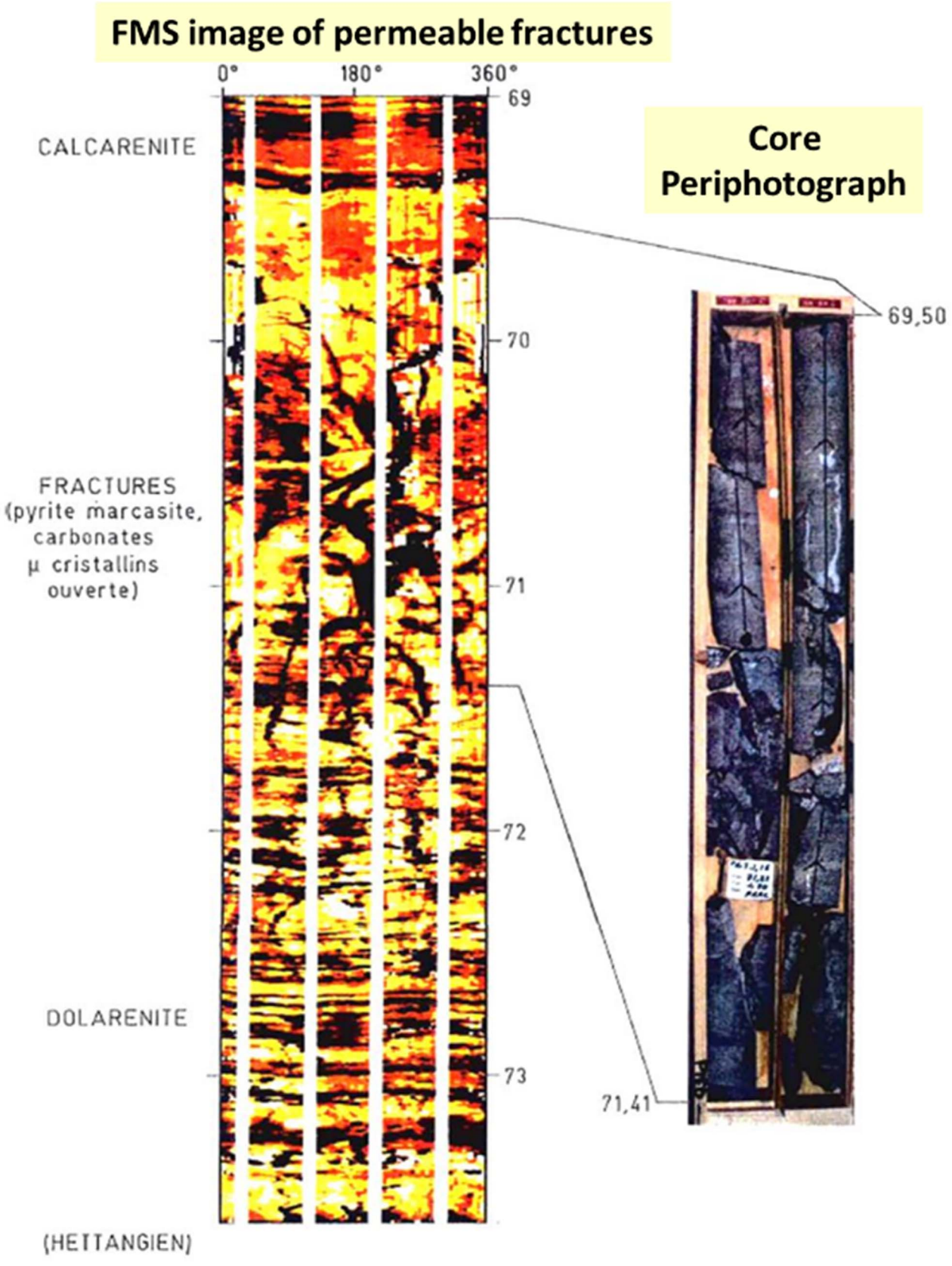

Fig. 12. GPF-Ardèche, MM1 borehole wall images and core periphotographs, 69–73 m.

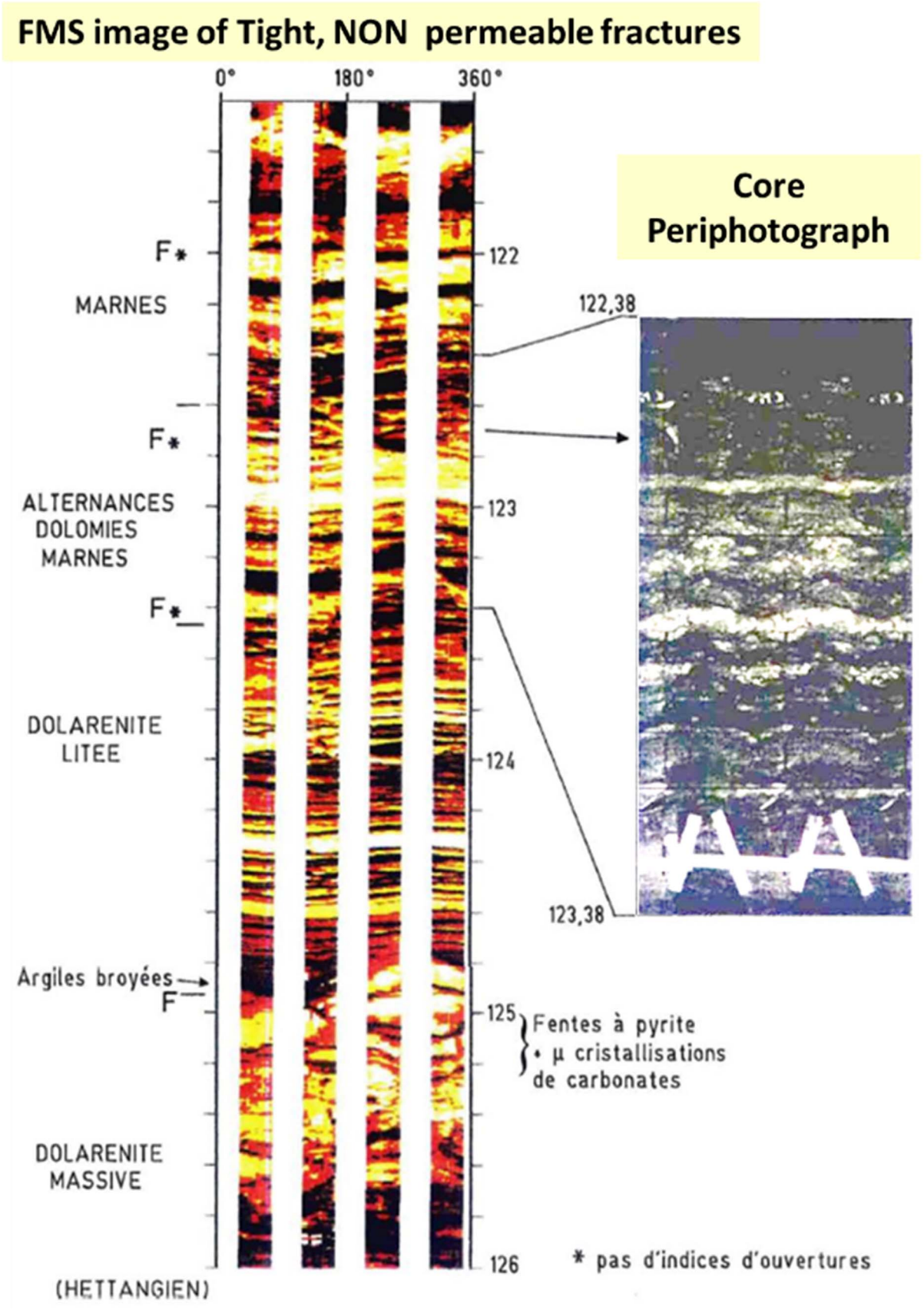

Fig. 13. GPF-Ardèche, MM1 borehole wall images and core periphotographs, 121–126 m.

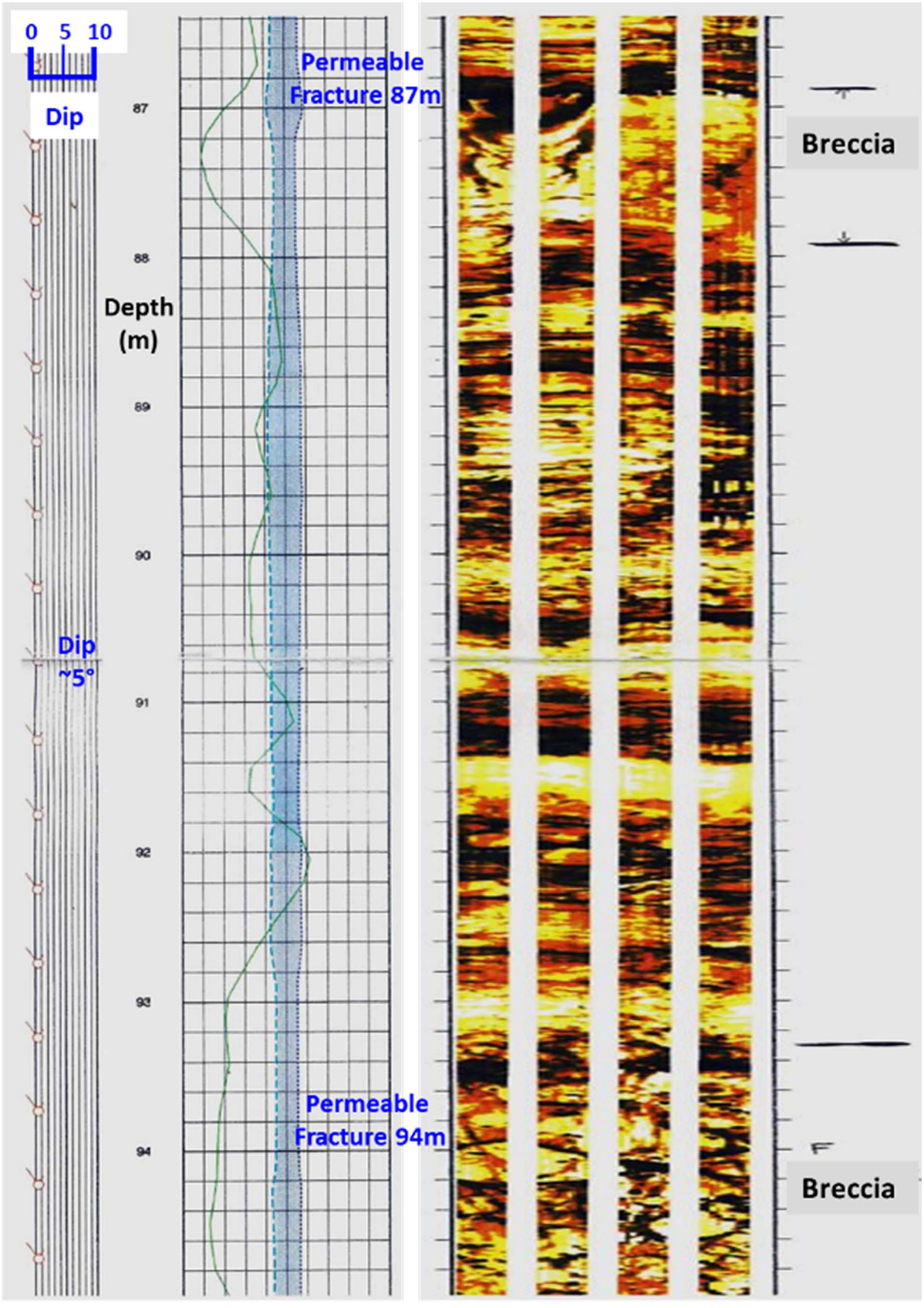

Fig. 14. GPF-Ardèche, MM1 hole, dipmeter, GR, FMS image of permeable fractures, 86–95 m.

4 is undefined, although the seismic dip toward NW around 250 m is in agreement with the dipmeter log results. *Thus, the S-wave splitting anisotropy results can be considered independent from the layering.*

The structural survey of the Hettangian formation exhibits a low level of fracturing, except for the very early and quasi-systematic brecciation of dolomites with shaly fillings and limestone cementing of fractures. Right along locally peaking S-wave anisotropy values revealed by the Dipole sonic DSI tool, the Hettangian reveals definite permeability hints: presence of micro-crystal carbonate deposits covering the fracture walls, or millimetric subvertical slits with discontinuous cementation (*e.g.* 94 m, FMS image on Fig. 14).

2.5 Additional elements of interpretation

The peaks of the velocity anisotropy ($\Delta V/V$) curves on Figures 10a–10c appear as sharply localized, with a minimal apparent peak to peak period of about 1 m in vertical depth: the vertical resolution of the applied S-wave anisotropy detection method by Rotation-Scan can thus be estimated to 0.5 m, *i.e.* half the receiver array span.

Non fractured conglomerates impregnated with heavy oil have been observed on cores around 252–253 m (Michel Degouy, BRGM, personal communication), and also correspond to a local peak of S-wave anisotropy (20%).

In the 89–91 m depth interval where a moderate amount of anisotropy is expressed, it is possible that a fracture is present close to the well but does not intersect it since the anisotropy level cannot be explained by the unfractured core aspect or by any locally deviated value on all other logs.

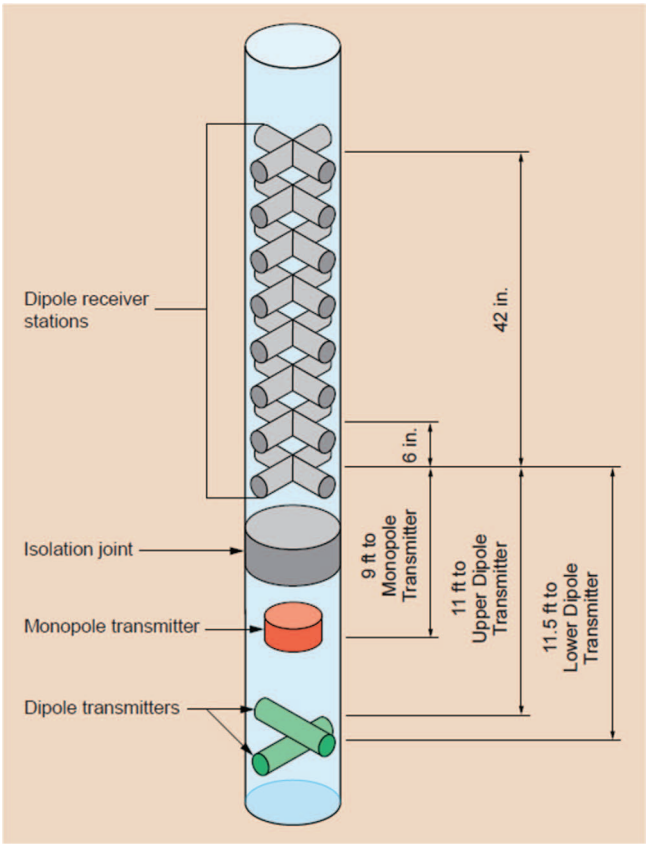

Fig. 15. DSI: Dipole Shear Sonic Imager Tool, from *Figure 3 of Belaud and Standen* [9]. The dipole section of this tool consists in an array of eight dipole receiver levels, and two orthogonal dipole sources.

3 Dipole sonic recording configuration and processing results (1993–1994)

3.1 DSI Dipole sonic tool and field operation

A sketch of the DSI tool is shown on Figure 15, modified from Belaud and Standen [9], in which the field acquisition cycle is described. In MM-1, the "Both Cross-Dipole" acquisition mode was activated, meaning that the array of 8 levels of receivers X then the 8 orthogonal receivers Y were recorded SUCCESSIVELY for each of the successive emitted signals EX and EY, resulting in a 4 record cycle over each 1/2 foot depth interval, 40 μs sampling rate.

For the acquisition of dipole S-wave data, the sonic tool must be oriented, so that the processing results can be later referenced to the geographical North. In the present MM-1 well survey, a General Purpose Inclinometer Tool (GPIT, see Footnote 1) orientation element has been combined with the DSI sonic tool, enabling to read directly the Magnetic north in the open hole. If DSI data are collected in a cased hole, the low (2°–3°) well deviation measurements can be combined to the previously measured well trajectory order to orient the DSI data with the same Hole Azimuth (HAZI) angle.

The DSI processing procedure was initially commercialized by *Schlumberger* around the end of 1994, after Esmersoy *et al.* [10], and consists in detecting the eigendirections of S-wave propagation between the source location and the receiver array (11 ft–14.5 ft spacing, Fig. 15), the source signal being considered linearly polarized in the formation at source level. This detection algorithm is inspired by the method initiated in 1986 by Robert Alford [11], for S-wave surface seismic azimuthal anisotropy detection, using a fleet of horizontal vibrator trucks as a source.

Actually, the borehole wall can be rugged, caved, and fractures intersecting the borehole in an asymmetric manner could alter the mechanical parameters of the formation right at the level of the dipole sonic transmitter (Figs. 15 and 16), so that the linear signal polarization imparted on the opposite sides of the borehole wall at the transmitter level could be altered, however such effects are neglected in the "Alford" method hypothesis.

In the early 1990's, when the first dipole DSI sonic logs were recorded in well MM-1 and in other wells, no commercial processing method existed yet, so that *Schlumberger-France* and *IFP* considered building an S-wave anisotropy prototype detection procedure based on an azimuthal S-wave slowness measurement Scan (Rotation-Scan), tentatively implemented as an independent experimental processing approach. Instead of re-writing from scratch a

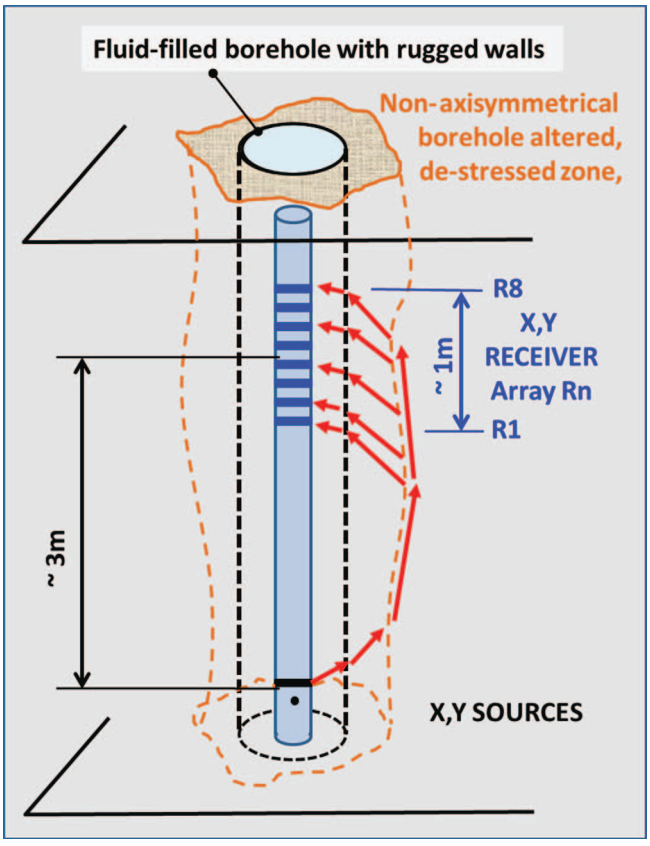

Fig. 16. Dipole Array Sonic tool in the borehole. Two birefringence detection processing routes: A) Alford type, $4x$ Rn response signal detection between source and mid array positions (~3 m). B) Azimuthal slowness measurement scan over the Rn array interval only (~1 m), independently for the azimuths of linearly polarized VS-fast and VS-slow principal shear modes.

computer anisotropy detection routine for the dipole sonic signals like the one developed by Naville [12] for oriented 3C VSPs, the authors took advantage of the existing industrial STC slowness computation method in order to measure the sonic S-wave velocity in a large range of azimuthal directions.

Therefore, the Rotation-Scan method consists in measuring the sonic S-wave velocity over the short DSI reception array (8 receivers, 0.5 ft apart, about 1 m array length), ref. sketch on Fig. 16, in a 180° range of incremental azimuth directions, 10° or 5° step, using the common Slowness-Time-Coherence (STC) routine available at the time [5]; then the azimuths of maximal and minimal S-wave velocity (or slowness) can be extracted from the scanned STC results. This method makes no assumption either on the polarization shape of the actual source signal sweeping through the 1 m long receiver array, or on the homogeneity of the rock formation located between the source position and the receiver array position, about 3–4 m apart (Fig. 16). It only assumes that the principal shear waveforms remain in constant shape over the receiver array, meaning that the rock formation is considered homogeneous with the same anisotropy directions over the receiver interval, even if different layers are present.

Table 1 was established in late 1997 to summarize the differences between the Alford-based detection routine described in Esmersoy *et al.* [10] and commercialized during 1994, and the Rotation-Scan one. *With the Alford routine*, the detection occurs over the space distance between the transmitter/source and receivers, encompassing the receiver array *i.e.* about 3–4 m over which the principal S-wave directions are assumed to be unique, and *the formation is assumed homogeneous in the Transmitter-to-Receiver interval,* while *the Rotation-Scan detection* is performed over the short span of the receiver array (nearly 1 m) and *assumes the formation homogeneity only over the shorter 1 m receiver array span,* resulting in a higher resolution and an improved accuracy of the S-wave anisotropy results.

Actually, the computed slowness anisotropy results obtained by the Rotation-Scan indicate that the presence of permeable, thus open fractures are marked by high velocity anisotropy, while closed, cemented fractures show weak anisotropy; these results are confirmed by the examination of the corresponding cores.

3.2 Comparison between Anisotropy results of both detection methods

Figure 17a displays the results of the Alford commercial S-wave detection routine applied in the 170–220 m interval of MM-1 borehole.

- Track 1: Quality index of anisotropy detection: min and max Cross-ENERGY of the signal recorded in directions orthogonal to in line emitted signal, colored in green between the two curves: a null Min-Energy means that for one of the principal S-wave, there is NO energy received orthogonally to the emitted in-line S-wave azimuth, which automatically indicates that the emitted S-wave polarization is imparted linearly into the rock formation of the borehole wall at the transmitter level, with nearly cylindrical, borehole wall geometry, and without major heterogeneity nearby. A large Max-Energy means that the hole environment is either anisotropic, or heterogeneous; "*a small Min-Energy associated with a high Max-Energy is a reasonable indicator of the presence of S-wave anisotropy, in agreement with the model and its assumptions*", as expressed by Esmersoy *et al.* [10].
- Track 2: DSI tool EX upper dipole transmitter Azimuth (smooth dashed curve, 0–360°), Gamma rays (high frequency solid and dashed–point curves), Correlation coefficient between the two principal waveforms in the signal computation window, in green on right side of Track 2 (the Correlation coefficient looks always higher than 0.99; the computation window is shown in Track 5).
- Track 3: Principal Fast S-wave azimuth, scale −180° to 180°: (solid black log), surrounded with an azimuth uncertainty orange ribbon, about ±5° to ±10°. The S-fast and S-slow azimuths are assumed to be orthogonal.

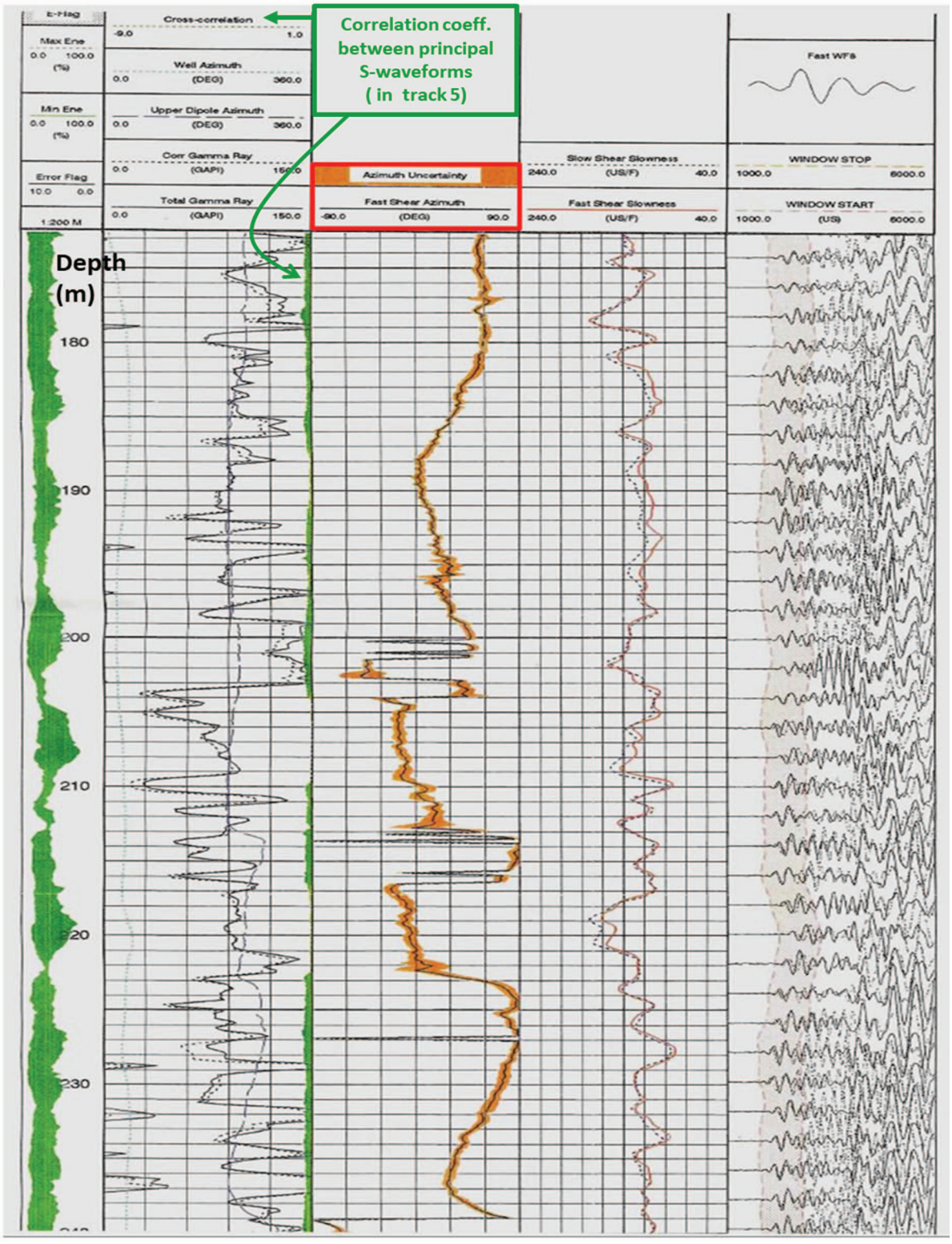

Fig. 17a. GPF-Ardèche, MM1 borehole: Alford-type Process anisotropy results, 173–240 m. Track 1: Detection Quality: min and max Cross-ENERGY, green shade between the two curves. Track 2: Well azimuth and upper dipole EX azimuth (smooth dashed curve, 0–360°), GR (solid and dashed-curves), Correlation coefficient between principal waveforms (dashed green). Track 3: FSA/Fast S-wave azimuth, −180° to 180°: (solid black), surrounded with uncertainty orange ribbon, ±10°. Track 4: DTS slowness 40–240 µs/ft, DTSmin (red) and DTSmax (Black dashed) outputs. Track 5: Fast-S Waveform (solid wiggle) on receiver 8, Slow-S Waveform (dashed wiggle signal) on receiver 7, and shadowed computation window.

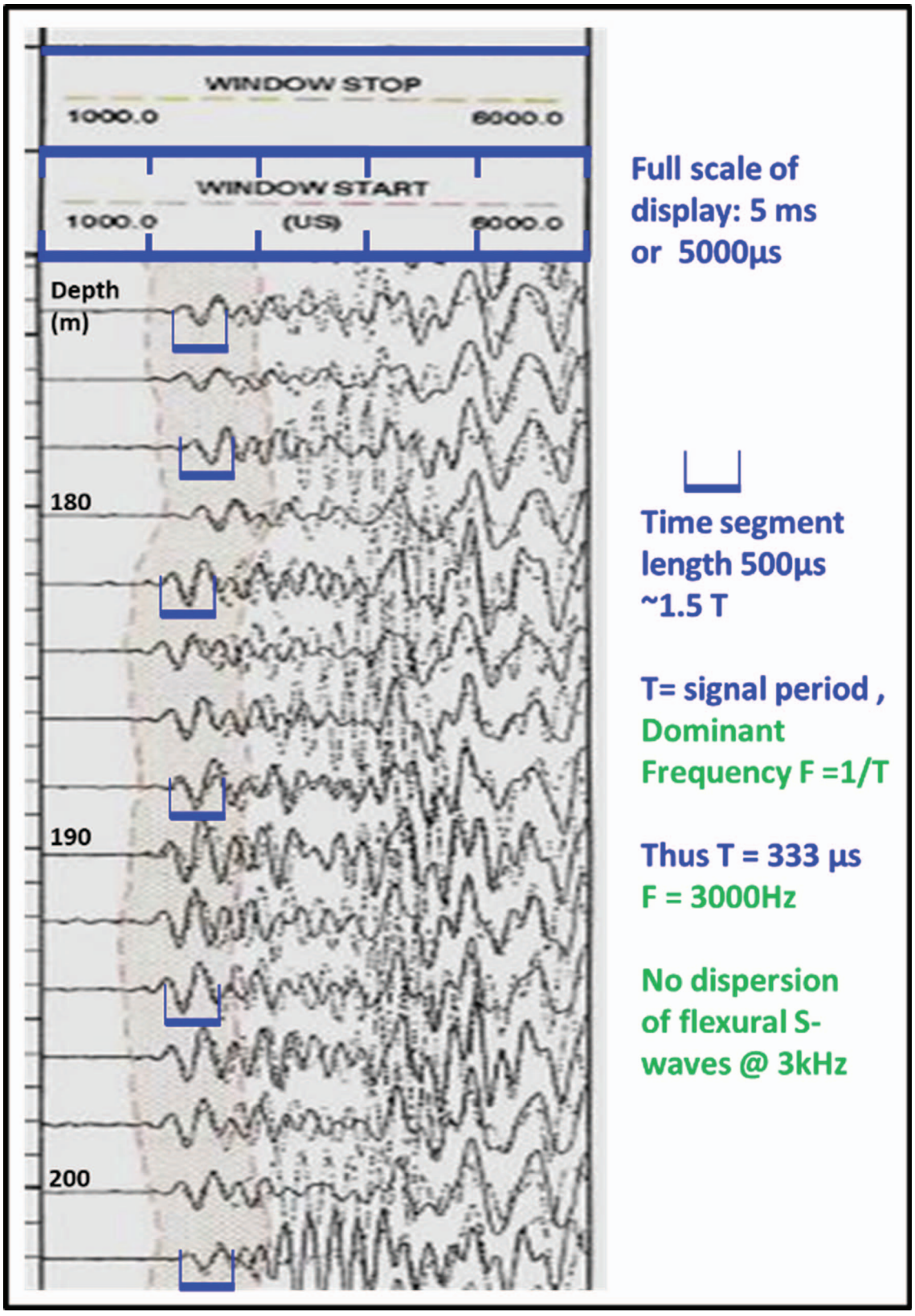

Fig. 17b. GPF-Ardèche, MM1 borehole: Principal S-waveforms output from anisotropy detection on DSI data. Enlarged from Figure 17a. The dominant frequency of the processed DSI data is around 3 kHz; *Vs* velocities around 3000 m/s; Shear wavelength about 1 m.

- Track 4: DTS slowness logs 40–240 μs/ft scale: DTSmin (solid red line) and DTSmax (Black dashed line) output from Alford anisotropy detection process.
- Track 5: Fast-S Waveform (solid wiggle signal) on receiver 8, superimposed with Slow-S Waveform (dashed wiggle signal) on receiver 7, and shadowed computation window along and over the direct S-wave signal.

These initial results were produced in October 1994, at a time when the Alford algorithm implemented by Esmersoy *et al.* [10] and his *Schlumberger-USA* colleagues was still in its early development stage, as the Fast S-wave azimuth log exhibits many flips of 90° where the azimuths of principal S-fast and S-slow waves appear suddenly exchanged along the depth axis. Although this visible S-wave computational azimuth uncertainty has been seemingly reduced after 1995, we will mainly examine the results in the depth intervals where the Fast-S azimuth remains quite stable.

Figure 17b is an enlargement of the principal S-waveforms from Figure 17a, pinpointing the dominant frequency of the S-wave signal, around 3 kHz: it indicates that the S-wave anisotropy detection performed on the raw recorded DSI signals relates to the low frequency segment of the flexural wave dipole signal, which velocity is now known to fit with the S-wave velocity of the body waves in the formation. Therefore, the low amplitude dispersive higher frequency part of the flexural wave spectrum can be neglected.

Figures 10a–10c display the S-wave velocity anisotropy detection results from the Rotation-Scan algorithm, however without the azimuths of the principal fast S-wave and Slow S-wave determined during the computer detection run.

In order to produce comprehensive velocity anisotropy results, the azimuths of S-fast and S-slow were sorted from the Rotation-Scan computed results, and displayed on Figure 18, exhibiting, left to right:

- Track 1: max/min C1/C2 diameters from 4 arm Caliper, in red, and Gamma Ray (GR) in green: the hole was enlarged to 6″1/4 before running the DSI tool, and there is quite no detectable ovalisation after hole diameter enlargement, in spite of an actual diameter between 7″–7″1/2.
- Track 2: Principal S-wave azimuths, scale −180° to 180°: Fast Shear Azimuth (red), Slow Shear Azimuth (purple), AZimuth difference (Fast AZ minus Slow AZ) in magenta, and DSI tool (EX transmitter direction) Azimuth (blue, 0–360°).
- Track 3: right to left: slownesses 40–240 μs/ft scale: DTCO (green), DTSmin (red) and DTSmax (black), output from Rotation-Scan, DTS from UTX and LTX dipole transmitters (solid blue and dashed blue), $\Delta V/V$ curve (black, scale 10–30%).

Remark: the DTS values output from the STC routine applied to the UTX and LTX dipole transmitter emission data (solid blue and dashed blue curves), and on the raw shot collections of 8 receivers, appear to be either both intermediate between the DTSmin and DTSmax S-wave slowness values (solid black and red curves) output from the Rotation scan, or almost superimposed to the principal S-wave black and red slowness curves, *depending on the DSI tool azimuthal orientation* (blue curve on Track 2). As expected, when the DSI tool (X referenced direction) points to a principal S-wave azimuth (*i.e.* where the blue and red curve azimuths on Track 2 nearly fit, mod 90°), the UTX and LTX DTS solid and dashed blue curves on Track 3 coincide with the black and red anisotropic principal S-wave slownesses output from the Rotation scan; however, in the 210–220 m depth interval, very small azimuthal differences are observed between the DSI tool orientation and the fast S-wave azimuth (Track 2, blue and red curves), while the UTX and LTX S-wave DTS values from STC are almost identical and intermediate between fast and slow principal S-wave slownesses values on Track 3: *this observation shows that the detection of the anisotropic principal S-wave azimuths can be very sensitive locally, EVEN where the birefringence anisotropy is high*. The reason why the DTS slownesses were initially computed from the UTX and DTX receiver collections recorded on the field is that the processing petrophysicists desired to quickly verify the existence of any hint of S-wave velocity anisotropy in the MM-1 borehole, knowing that the DSI tool rotates as the wireline cable untwists during the logging run; if no difference would have been observed at any depth between the solid and dashed blue DTS slowness curves computed from the UTX and LTX raw data collections, the authors would have concluded that no S-birefringence existed in the MM-1 well, thus excluding any further processing action…

Therefore, the Fast-S and Slow-S azimuths can be compared in the common 170–220 m interval between the Alford method results (Fig. 17a) and the Rotation-Scan results (Fig. 18), they are displayed side by side on following Figure 19.

The principal S-wave azimuths from Rotation-Scan appear consistent with depth and in good agreement with the known tectonic stress oriented N30°E expected in a large well vicinity. Locally, flaps of 90° where the azimuths of principal S-fast and S-slow waves are suddenly exchanged occur most systematically where there is a large slowness contrast linked to layered lithologic changes; this occurs where the DSI receiver array lies over interfaces with high slowness contrasts, which alters the slowness values output by the STC process; time picking the S-wave arrivals could further improve the accuracy of results in these circumstances.

The lower (250–310 m) depth interval had been logged four times with the dipole DSI tool, with different tool azimuthal orientations for each run: the Rotation-Scan consistently found the same fast S-wave azimuth (±5°) over the four repeat sections (results not shown), which gives a good confidence in the whole S-wave birefringence acquisition mode and Rotation-Scan processing method.

This Rotation-Scan prototype test result was obtained by J.P. Yver in *Schlumberger-France* in 1995, unfortunately the method was not fully developed and implemented to commercial stage.

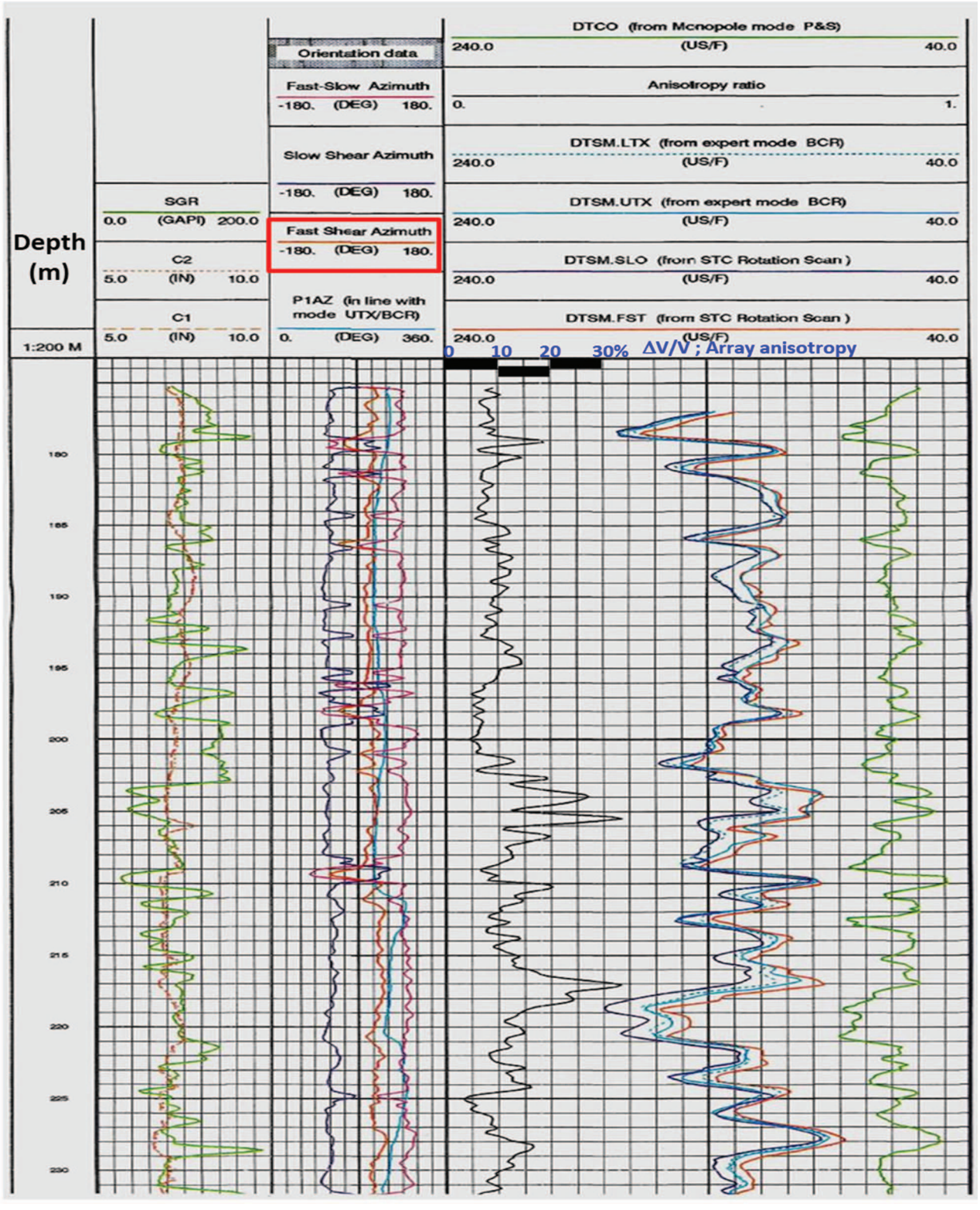

Fig. 18. GPF-Ardèche, MM1 borehole: Rotation scan anisotropy results, 173–232 m. Track 1: max/min C1/C2 diameters from 4 arm Caliper (red), GR (green). Track 2: Principal S-wave azimuths, scale −180° to 180°: FSA/Fast Shear Azimuth (red), Slow Shear Azimuth (purple), AZimuth difference (Fast AZ minus Slow AZ) in magenta, and DSI tool(EX) orientation Azimuth in blue, 0–360°. Track 3: slownesses 40–240 µs/ft scale, right to left: DTCO (green), DTSmin (red) and DTSmax (black) from Rotation-Scan, DTS from UTX and LTX dipole transmitters (solid and dashed blue), $\Delta V/V$ anisotropy curve (black), scale 10–30%.

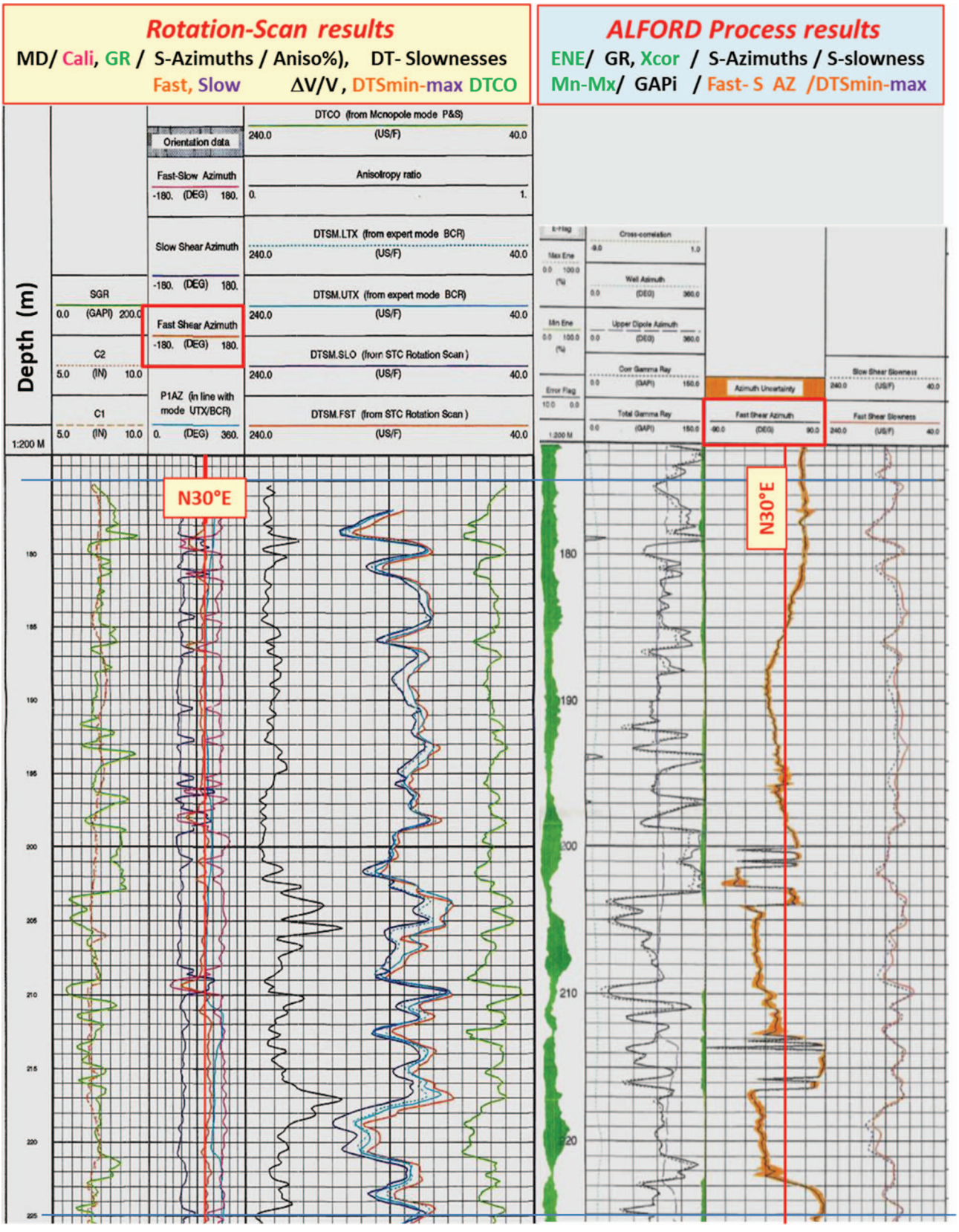

Fig. 19. GPF-Ardèche, MM1 borehole: Dipole sonic anisotropy results from both birefringence detection methods, in depth interval 173–225 m. The regional N30° E fault strike direction is drawn as a red line over the FSA/fast S-wave azimuth curve results from both detection methods.

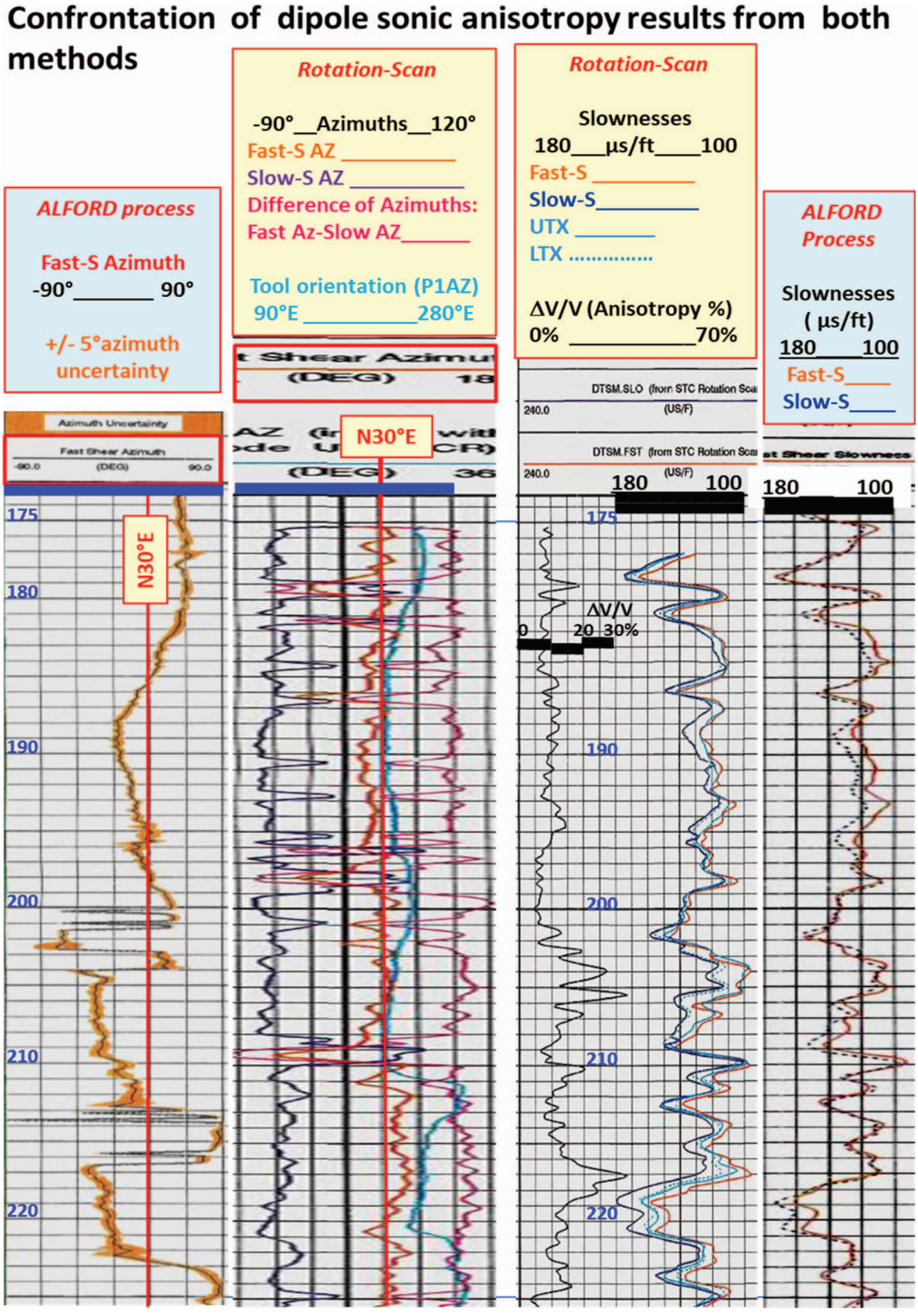

Fig. 20. GPF-Ardèche, MM1 borehole: Dipole sonic anisotropy results from both birefringence detection methods, same FSA/fast S-wave azimuth scale, same slowness scale, 173–225 m.

4 Detailed confrontation of anisotropy results between both detection methods (2021)

In order to properly compare more accurately the anisotropy processing results from both Alford and Rotation-scan routines applied to the same dipole sonic data recorded in the MM-1 well, Figure 20 has been assembled in the same 175–225 m depth interval with the S-wave principal azimuth axis and the fast/slow principal S-waves slowness logs displayed with identical respective Azimuth and slowness scales, showing:

- Track 1: *Alford process,* principal Fast S-wave azimuth, scale −90° to 90°: (solid black log), surrounded with an azimuth uncertainty orange ribbon, about ±5° to ±10°. The S-fast and S-slow azimuths are assumed to be orthogonal in the Alford process.
- Track 2: *Rot-scan process,* principal S-wave azimuths, scale −90° to 120°: Fast Shear Azimuth (red), Slow Shear Azimuth (purple), AZimuth difference (Fast AZ minus Slow AZ) in magenta, and DSI tool/EX transmitter/ orientation Azimuth (blue curve, 90–280°, from combined GPIT tool).
- Track 3: *Rot-scan process,* right to left: slowness logs, 40–240 μs/ft scale: DTSmin (red) and DTSmax (black), output from Rotation-Scan, DTS from UTX and LTX dipole transmitters (solid blue and dashed blue), $\Delta V/V$ curve (black, scale 10–30%).
- Track 4: *Alford process,* DTS slowness logs 40–240 μs/ft scale: DTSmin (solid red line) and DTSmax (black dashed line) output from Alford anisotropy detection process.

Immediate observations can be expressed:

- The S-Fast azimuth from Alford process (Track 1) is very erratic *versus* depth, with estimated uncertainty ±5°, but with azimuth values often very different by up to 45° from the stable and coherent S-Fast azimuth obtained by the Rotation-Scan results (Track 2, orange log), mainly centered on N30°E, ±15°. The maximal horizontal stress can be derived from the N30° strike trend of the main regional faults, shown on Figure 2. In contrast, on Track 2, it is quite reassuring that the fast and slow principal S-wave azimuths are mostly orthogonal to each other, *although they have been determined independently* from each other during the rotation scan of STC slowness determination over the span of the receiver array. The erratic detection of the S-Fast azimuth yielded by the Alford algorithm could not be explained at the time despite the repeated detection runs carried out in the processing center.
- As a consequence, the differences between S-fast and S-slow slownesses shown in Tracks 3 and 4 (respectively Rotation scan process and Alford process) in the same 100–180 μs/ft scale range are quite inconsistent between the two methods, mainly where the fast-S azimuths differ by more than 15° between the two methods.

Depth enlargements of Figure 20 have been produced on Figures 21a–21c, calling for the following comments:

- Interval 175–180 m: weak Anisotropy (7–10%) from Rot-scan, is NOT FOUND by Alford.
- Interval 180–195 m: Similar results from both methods. *Rot-scan results are very sensitive to abrupt velocity variations within the DSI array, in which the slowness is assumed to be unique (Kimball and Marzetta, [13]).* The S-fast azimuth from the Rot-scan process is always found, in a coherent direction close to N30°E, while the S-slow azimuth is locally false or inaccurate, non-orthogonal to S-fast Azimuth: this effect could be the result of a stronger attenuation of the S-slow principal mode (to be verified). Between 179 and 180 m, the azimuths of S-fast and S-slow from Rot-scan are exchanged, remaining orthogonal to each other: a re-examination of the cores is recommended, as well as ultrasonic birefringence measurements on the corresponding core, to confirm this interesting result. A possible explanation could be that the dominant frequencies recorded by the DSI tool lie beyond the slowness cross-over point between slow and fast principal S-wave modes, an explanation to be carefully investigated. In contrast, the S-fast azimuth from Alford remains identical to the neighboring formations...
- 195–201 m: weak Anisotropy (5%). Similar anisotropy azimuth from both methods, although Rot-scan results are more accurate. Coherent S-fast and incoherent S-Slow azimuths at 196–196.5 m on Rot-scan results. This feature might mean that the slow-S wave mode is more attenuated, with lower S/N signal to noise ratio than the fast S-wave mode.
- INCORRECT to NO anisotropy detected in 202–209 m interval by Alford method, *versus* stable birefringence azimuth and large anisotropy (10–30%) from Rot-scan, with S-fast azimuth close to N30°E.
- Flipped/Exchanged orthogonal directions of anisotropy axes in 197.8–198.7 and 209–210 m, from Rot-scan; the S-slow azimuth points to N30°E (if true, this would be a totally NEW result, to be confirmed from birefringence measurements on oriented cores).
- In the thin in 197.8–198.7 m interval, the Alford process cannot find any anisotropy, although its S-fast azimuth is similar to S-slow azimuth from the Rot-scan process.
- 210–224 m: HIGH to SUPER HIGH velocity Anisotropy (10%–30%) from the Rot-scan process. Stable S-fast birefringence azimuths output from the Rot-scan process are in full agreement with local fault strike and Max. H-Stress. *Independently determined principal S-waves azimuths output from the Rot-scan process appear remarkably orthogonal (within ±10°), thus confirming the method validity.*
- 210–224 m: in contrast, the Alford process yields INCORRECT or UNDETECTED birefringence principal azimuths and anisotropy values which calls for an additional investigation.

Lastly, after determining the principal S-wave azimuths, the S-wave attenuation can be computed on each of the two S-wave principal modes, which is expected to constitute an additional prognosis of potentially permeable, open fracture, either through the differential S-wave attenuation

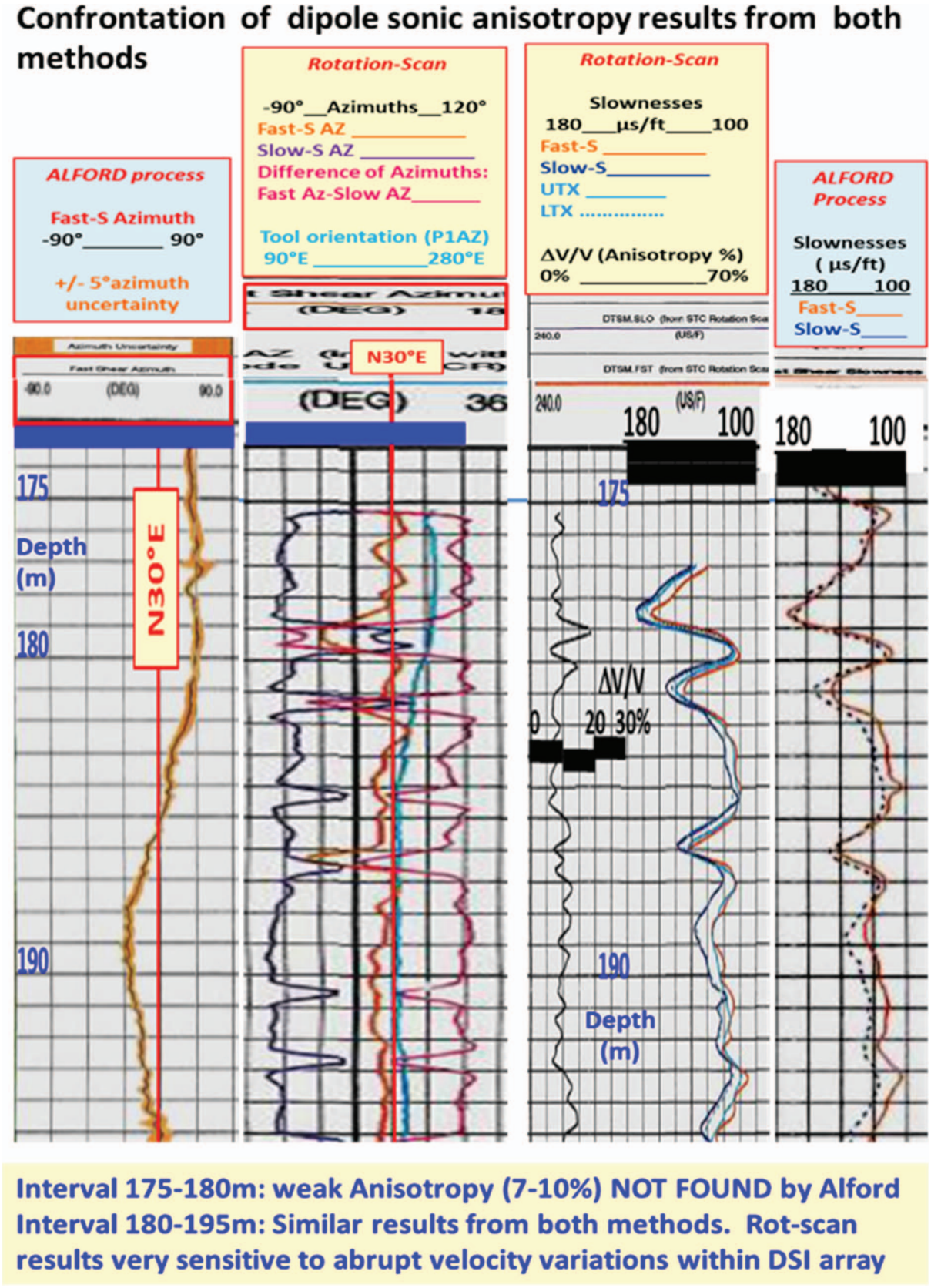

Fig. 21a. MM1 anisotropy results from both detection methods, same scale displays, depth interval 173–195 m, commented enlargement.

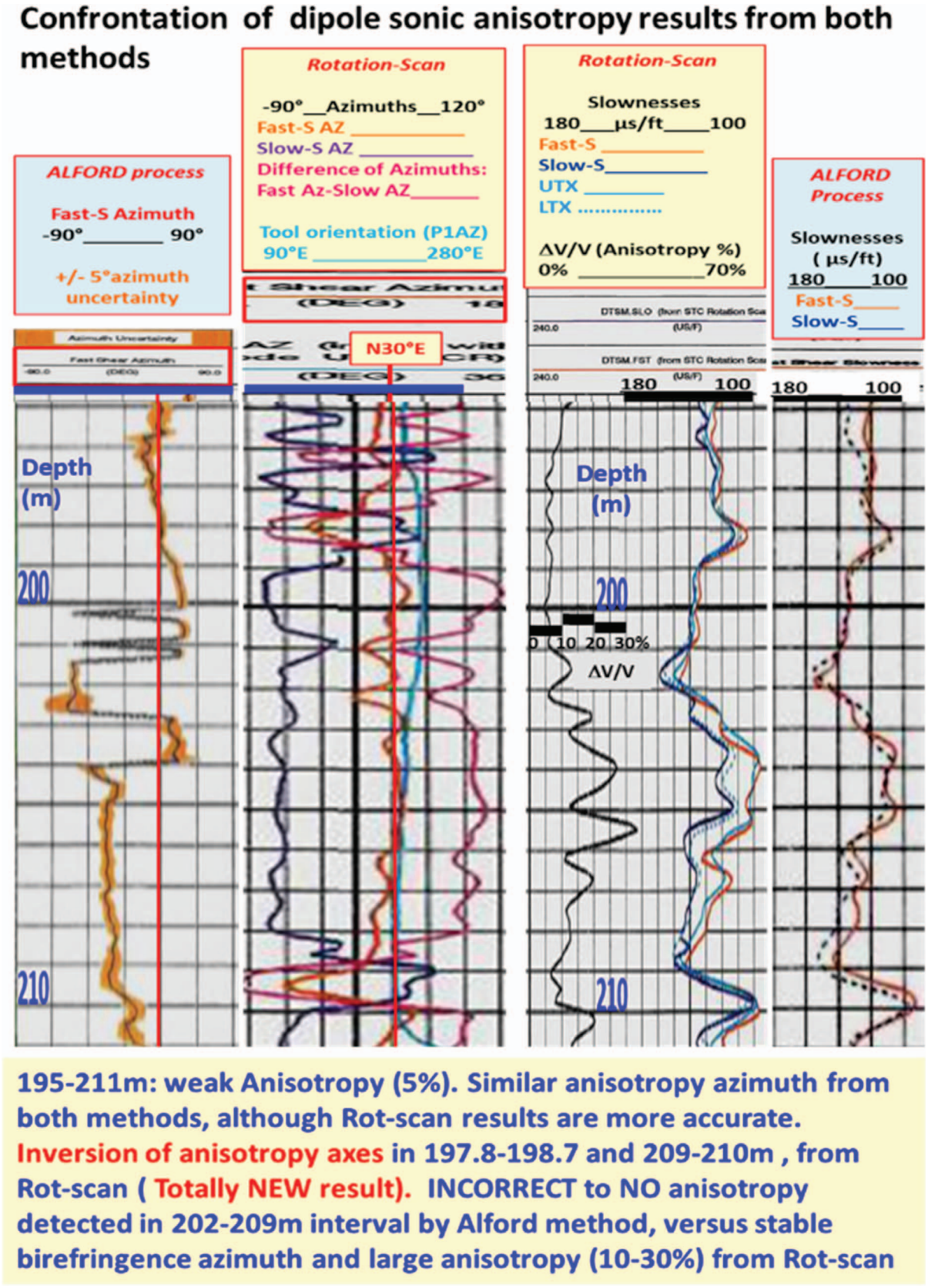

Fig. 21b. MM1 anisotropy results from both detection methods, same scale displays, depth interval 195–211 m, commented enlargement.

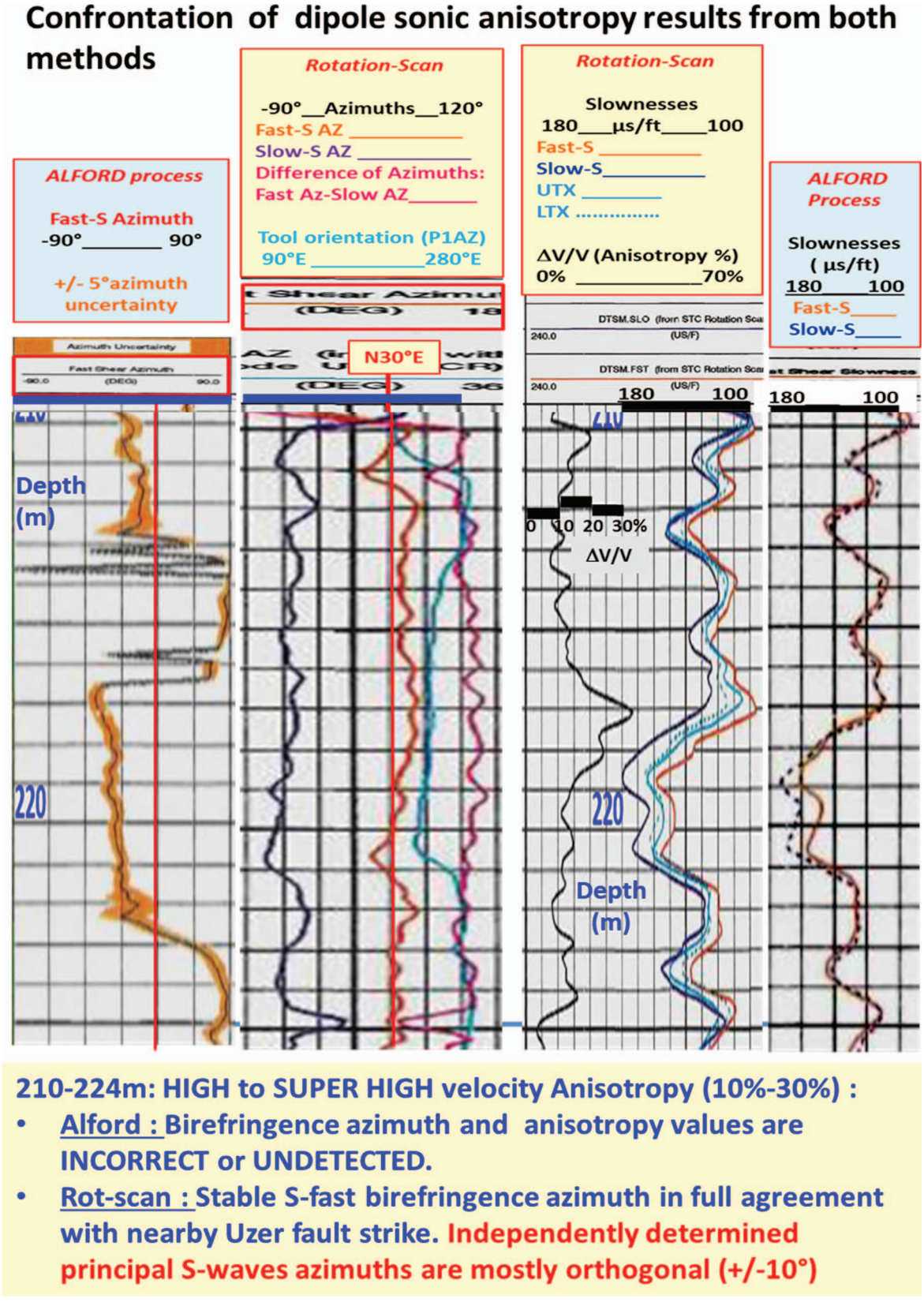

Fig. 21c. GPF-Ardèche, MM1 borehole: Dipole sonic anisotropy results from both detection methods, same scale displays, depth interval 210–224 m, commented enlargement.

anisotropy (QDs), or from a local increase of the absolute attenuation of the two S-waves (attenuations were not computed in the present study). Indeed, the S-wave attenuation strongly depends on the quality of the mechanical contact along the sides of a semi-open fracture. The sonic wave attenuation can be computed on each of the eigen S-wave modes in the same manner as on P-wave sonic arrivals generated by a monopole transmitter. Additionally, if NO velocity anisotropy is detected, it is possible to face a situation where the two principal S-waves (or flexural S-waves in the case of the dipole sonic) have different attenuations, in which case running an azimuthal computation scan of Shear wave attenuation (Att-Rot-Scan) along the direct S-wave arrival would be appropriate to detect the azimuthal S-wave attenuation anisotropy.

5 Discussion (2021)

5.1 On the altered/destressed zone surrounding the borehole

The comparative S-wave anisotropy detection results obtained in the present study help refining the understanding of the flexural S-wave generation at the S-wave transmitter level, and evaluating the validity of the hypotheses assumed when designing an S-wave anisotropy detection routine. Indeed, the hole ruggedness, the hole ovalisation, washouts and breakouts certainly alter the geometry of the borehole walls. Thus, there is no good reason to believe that the polarization of the S-wave imparted into a fractured borehole wall the level of a dipolar S-wave transmitter would *always* remain linear once it propagates into the rock formation. Additionally, there is a destressed zone around a drilled borehole, leading to an S-wave velocity decrease relatively to the virgin rock formation, within a diameter reaching up to three times the hole diameter. Also, drilling induced fractures near parallel to the well axis may occur. For instance, the geometry of the altered/destressed zone in the immediate borehole vicinity has been tacitly considered axisymmetric in the P-wave array sonic study by Bouchon and Schmitt [14], Coppens and Mari [15], in classical seismic refraction concepts to the flexural wave propagation; the hole geometry is explicitly defined as axisymmetric in the S-wave dipole sonic study by Hornby [16] and Tang *et al.* [17], applying tomographic inversion methods to the flexural wave time picks, yielding a map of the decreased velocity/destressed zone surrounding the borehole.

The axisymmetric assumption of the rock characteristics in the near borehole ensures that a linearly polarized shear pulse imparted orthogonally to well axis remains linear in the rock formation, however the borehole wall asperities do not favor this hypothesis.

The perturbed near wellbore region may also be anisotropic, and the principal flexural S-wave have differing dispersion characteristics (Plona *et al.* [18]), so that the axisymmetric assumption of this near wellbore zone might be approximate for very damaged borehole wall situations.

In the present MM-1 coredrill case, the perturbed near wellbore can simply be locally heterogeneous, without any symmetry, especially in front of fractures (*e.g.* Fig. 12).

It is quite interesting to observe the effects of hydraulic fracturing in a borehole, increasing both the S-wave birefringence anisotropy and the radius of the destressed zone surrounding the well, as illustrated by Su *et al.* [19].

Remark on the radius of the destressed zone around a borehole: The near wellbore region perturbed by the drilling process is reported to extend 2–3 borehole diameters into the formation before sensing the unaltered rock by low frequency cross dipole sonic shear waves (Plona *et al.* [18]). In coal mines, when a reconnaissance gallery is dug by hand and peak, the destressed radius is reported to extend up to three times the gallery radius; when the gallery is dug with explosives, the destressed diameter can reach up to five times the gallery diameter, due to the fracturing shock waves generated by the explosives. The *Houillères de Lorraine (HBL)* coal mine engineers were exploiting highly dipping coal seams, and they noticed that destabilized coal blocks slid into the gallery sometimes, from a distance equal to what they assumed to represent a "destressed radius distance" from the gallery, which length depended on how the gallery was dug (personal communication). Very likely, the destressed zone radius around the borehole can differ depending on the borehole being cored, or rotary drilled, or hammer drilled, and on the mud pressure applied during the drilling process; the same geomechanical destressing occurs around large diameter tunnels...excavated with a boring machine, *versus* bored using explosives.

5.2 On the assumptions made by diverse velocity anisotropy detection methods and algorithms applied to dipole sonic datasets, influencing their reliability

The method initiated by Alford [11] looked like a good start for the S-wave velocity anisotropy detection, assuming identical principal S-wave directions in the whole spacing between transmitter and receiver array, and linear polarization imparted to the rock formation at the transmitter depth level. The same method has been improved by Tang and Chunduru [20], and these authors have obtained a higher anisotropy rate resolution when the array slownesses of S-fast and S-slow waves were computed in the azimuthal directions detected with their anisotropy parameter inversion algorithm.

In the recent paper by Market *et al.* [21], the anisotropy detection algorithm called "Azimuthal semblance" seems to be exactly the method implemented in the present study by J.P. Yver, yielding results very similar to the "Minimization Energy method" developed by Esmersoy *et al.* [10], which means that the quality of the anisotropy detection methods might be data-driven, depending on the geology and on the borehole conditions. Market *et al.* [21] accurately point out in pages 6–7 that:

> "Alford rotation should be used with the following caveats in mind: ...it will not work well in non-symmetrical cases such as a bed boundary crossing, inclusions, etc.".

Table 1. Comparison of S-wave birefringence detection methods.

	Alford-type method T-R ANI (Algorithm-1)	Azimuthal DTS Rotation-Scan Array ANI (Algorithm-2)
PRINCIPLE	Minimizing cross dipole energy, or minimizing the off-diagonal elements of the 4-term matrix of the Source(s) to Receiver(r) signals(XsXr, XsYr, YsXr, YsYr).	Scan of S-wave slowness/velocity over 180° azimuth range, to *INDEPENDENTLY* determine the azimuths of Vs-max & Vs-min
ASSUMPTIONS	The propagation medium between Transmitter to the Receiver array is considered homogeneous, with same anisotropy axes, possibly stratified axisymmetric.	The propagation medium is considered homogeneous over the Receiver array ONLY. The SHORT detection interval yields a higher depth resolution
	Emitted flexural S-wave particle motion remains LINEAR in the borehole formation located in the immediate source vicinity.Equal orthogonally emitted signals, in same shape, same amplitude	No polarization constraint: Emitted S-wave imparted into the formation can be in any form, LINEAR, ELLIPTICAL, CIRCULAR... Orthogonally emitted signals may be a bit different.
For BOTH methods:	The borehole ruggedness and heterogeneous borehole altered zone over the detection depth interval may alter the accuracy of results	
	Differential attenuation (QDs) between the two principal S-wave modes is NOT considered	When NO velocity anisotropy is detected, a scan of S-wave attenuation (Att-Rot-Scan) *versus* azimuth can be run to yield the S-wave attenuation anisotropy & the Differential attenuation (QDs)
Observed RESULTS	Fast-S-wave Azimuth is searched FIRST, resulting in INACCURATE to FALSE principal S-wave principal azimuths when hypotheses are unsatisfied, or in case of weak S-wave anisotropy.	Fast-S-wave Azimuth is derived from the azimuthal STC slowness scan, resulting in higher azimuth accuracy of principal S-wave modes, and higher depth resolution. STC routine could be improved where the receiver array is located over a strong velocity contrast.
	The borehole ruggedness and heterogeneous borehole altered zone over the detection depth interval may alter the accuracy of results. The larger the detection interval, the larger potential bias...	

By design, in deviated and horizontal wells, any anisotropy detection method cannot separate directly simultaneous causes of anisotropy and complementary modelling should be considered (Hornby *et al.* [22]), as secondary and dominant anisotropic causes are not separable.

The waveform inversion proposed by Blanch *et al.* [23] aims to "*decouple the estimation of Fast and slow shear wave, ... which are considered having different propagation properties, such as attenuation and dispersion*", adding that "*The deviation from a 90° difference between the two angles is used as an error estimate*". However, the theoretical inversion process described by Blanch *et al.* [23] ignores the differential attenuation effect and the lower signal to noise ratio for the more attenuated principal S-wave; nevertheless it illustrates an approach similar to the azimuthal rotation STC scan implemented by J.P. Yver in the present case study, summarized in Table 1.

Estimating the reliability of an S-wave anisotropy detection method is difficult where the assumptions of the detection algorithm are not respected, especially when the symmetry of near borehole geomechanical parameters around the hole axis is absent, for instance where the ruggedness of the borehole wall is important, or where open fractures intersect the borehole. Although the Fast principal S-wave azimuth appears consistently oriented around N30°E on the Rotation-Scan results (Fig. 20), the most plausible explanation for the erratic fast S-wave obtained by the Alford–Esmersoy method [11] seems to be the depolarization of the linear source particle motion when the transmitter faces a mechanical heterogeneity on the borehole wall, or when a mechanical heterogeneity is present between the source and the first receiver (Figs. 16 and 22).

Many researchers investigated the response of a stack of several media with different anisotropy axes, as illustrated for instance by Figures 13 and 14 of Sondergeld and Rai in their ultrasonic laboratory observations [24], where a stack of two media with different anisotropy azimuthal axes and characteristics is considered: the principal S-wave polarizations received after propagation in the second

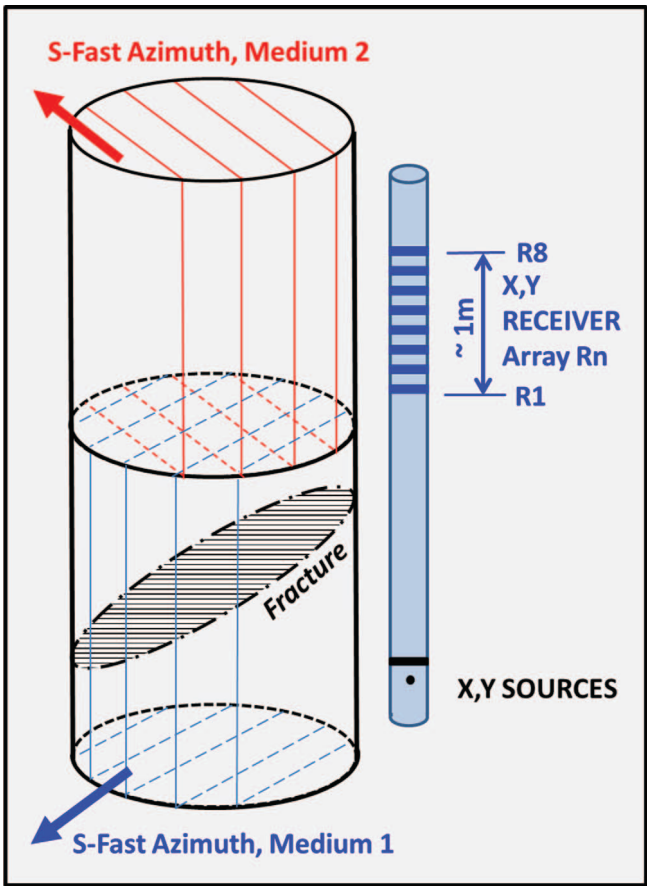

Fig. 22. Inhomogeneous anisotropy *versus* depth: when the direction of anisotropy axes *versus* depth varies, and/or if a heterogeneity is present between the emitter and closest receiver R1 of the dipole sonic tool, the measured birefringence relates ONLY to the medium facing the receiver array, (medium-2), independently from the prior S-wave propagation in medium-1 (ref. *Figs. 13, 14 of Sondergeld and Rai* [24]).

medium are INDEPENDENT from the polarization of the incident S-wave train propagated in the first medium of propagation, and independent of the source signal polarization as well.

Accordingly, Figure 22 illustrates a two media situation where the anisotropy axes are possibly different between the dipole emitters and the proximate receiver R1, possibly including a local formation mechanical heterogeneity such a complex fracture surface which may randomly depolarize the S-wave particle motion. In this case, the array of receivers records the propagation effects of the ONLY medium in which they are located.

Consequently, the only hypothesis requested to run an STC velocity measurement is that the depth interval facing the dipole sonic receiver array be fairly homogeneous, as recalled on the right side of Table 1. Of course, in heterogeneous formations, the propagation medium is less likely to have stable anisotropy axes over a long spacing (3.5 m for the DSI source to receiver array geometry) than over the receiver array only (~1 m).

S-wave depolarization of a linear motion imparted by an S-wave source is often observed on shallow direct S-wave arrivals of onshore VSP's recorded with a single horizontal vibrator, although this effect is not systematic and depends on the heterogeneity of the near surface weathered zone and shallow layers. If the above explanation is confirmed by future dipole sonic borehole surveys using several S-wave anisotropy data processing methods, the geomechanical geoscientists and the drilling engineers might be interested in the Alford–Esmersoy algorithm results as an indicator of the borehole wall mechanical heterogeneity, even where the borehole wall geometry is nicely cylindrical...

5.3 On the plausibility of the high velocity anisotropy magnitude evidenced at the depth levels of confirmed permeable fractures in the MM-1 coredrill using a simple Rotation STC scan method

In a remarkable paper by Zhuang *et al.* [25], a highly anisotropic HTI physical model of sizable dimensions (3.5 m diameter cylinder, 10 m high, with a hole in the center) has been deliberately constructed in order to evaluate the existing anisotropy measurement hardware tools, followed by the application of various anisotropy processing procedures. The authors state:

> The model consists of a series of equally spaced thin limestone slab sheets cemented with concrete, resulting in a transversely isotropic medium. For the anisotropy measurement evaluation, the borehole model is tested by a standard multipole acoustic tool. The measurement finds an *S-wave anisotropy magnitude about 20%* and determines the fast S-wave polarization along the alignment direction of the slab sheets. The results of the work not only validate the borehole measurement technology, but also provide a testing facility for calibrating the measurement acoustic tool.

Not only the anisotropic physical model and surrounding facilities described by Zhuang *et al.* [25] offer a very convenient test bench to evaluate the commercial sonic tools, but the reported magnitude of S-wave velocity anisotropy of 20% confirms that the 30% peak values of velocity anisotropy observed in the MM-1 well right at 0.5 m high permeable fractured intervals are realistic. This observation definitively enlightens the phenomenon of differential attenuation between Fast-S and Slow S-waves across open fractured borehole short intervals, a subject still overlooked by the commercial dipole sonic service companies, let alone ignored by academic researchers, despite the published examples of differential S-wave differential attenuation results obtained in several converted P-S wave/3-Component surface seismic surveys.

A more recent case study evidences a high S-velocity anisotropy magnitude of about 30%, consistently high along a deviated well of the "case history #4", in a very low velocity shale formation, associated with a consistent S-fast azimuth (Kessler and Varsamis [26]). The geological context is obviously totally different than the one encountered

in Ardèche, and the MM-1 well is vertical, with subhorizontal surrounding layers.

In order to confirm the acoustical S-wave anisotropy results (azimuth, velocity and attenuation anisotropy) obtained from the dipole sonic logs, it would be desirable to measure the S-wave acoustical birefringence parameters using oriented ultrasonic shear sensors on an oriented rock plugs extracted from the oriented cores, as shown in Humbert *et al.* [27], in the cored borehole through the Chelungpu fault where DSI measurements have been conducted, as reported in Hung *et al.* [28]. Of course, laboratory anisotropy measurement can be achieved only on competent rock core samples which are retrieved from the borehole as an unbroken, solid cylinder. Despite this mechanical limitation, such S-anisotropy results from core birefringence analysis would help ascertain the accuracy and reliability of various dipole sonic signal processing algorithms, which may actually depend on the geological formations and on the borehole conditions (geometry, drilling induced fracturing, washouts, breakouts, heterogeneities *versus* homogeneity, etc.).

In this respect, several cored and fully logged borehole drilled in different geological contexts could be implemented as testing facility for calibrating the measurements and processing procedures of modern multipole/multi-source/multi-receiver acoustic tools, for the general benefit of the industrial and academic end-users. The open hole shallow MM-1 coredrill would have been a good test hole candidate (vertical coredrill in near horizontal layers, competent rock, no ovalisation, no fractures induced by drilling, no breakouts). The accessibility of the MM-1 coredrill will be verified.

5.4 On the necessity for the end-user interpreter-geologist to be aware of the various capabilities offered by the array dipole sonic tools and their limitations

The experimental dipole sonic survey in MM-1 coredrill, acquired with one of the first DSI commercial sonic tool, benefited from excellent field and borehole conditions, and excellent geological borehole information. Unfortunately, the extended time delay to produce processing results from the field DSI dataset, combined with the unexplained discrepancies observed between the results of two processing procedures applied by distant *Schlumberger* services caused a fading interest of the geologists and geoscientists in the early 1990's.

The quality of the DSI tool used in the MM-1 coredrill cannot be reasonably put into question to explain the discrepancies of the anisotropy processing results yielded by the two methods carried out by *Schlumberger*. The array sonic tools have been manufactured and commercially operated by *Schlumberger* since 1984 (Morris *et al.* [29]), and the performance of the hardware multipole sonic tool and anisotropy processing routines have been continuously improved, as attested by the comprehensive publications issued from 1998 to 2015 ([30–32]).

Nowadays, in order to complement and fulfill his exploration objectives, the end-user geoscientist engaging into a dipole sonic survey can benefit from an extensive amount of published papers on this technique, as dipole sonic tools are available from a variety of service companies. Additionally to the S-wave velocity measurements, a wide range of specific applications emerged for oriented multipole sonic tools: S-wave birefringence applied to stress determination, fracture detection/characterization, and 3D S-S reflection imaging within the 40 m radius borehole vicinity, including in cemented cased holes (Tang [33]).

5.5 On the importance to the interpreter-geologist and reservoir engineer to obtain reliable S-wave birefringence results, to identify its main driving origin, and to evaluate its relationship with palaeo-stress and present stress

In their study of the palaeo-stresses inferred from macro and microfractures on the cores collected in the deep Balazuc-1 borehole located in the hanging wall of the major Uzer fault, Martin and Bergerat [5] described the regional geodynamic setting, page 673:

> *The principal stages in the tectonic evolution of this region are well known and enough micro-tectonic data exist to be able to place the successive regional stress fields in their geodynamic context (Fig. 3).*

This latter figure has been modified in Figure 23 of the present paper so as to facilitate the local geodynamics understanding in the shallow MM-1 borehole, where the Hettangian formation of the upper Dogger is outcropping at the top of the footwall of the Uzer fault (Figs. 2–4).

In page 674, Martin and Bergerat [5] pursued:

> *A long period of extensional regimes followed, beginning during the Permian with NW–SE to N–S extension on the Cévennes border (Blès et al., 1989), which created or reactivated mainly E–W and NE–SW normal faults.*
> *The extensional regime continued during the Triassic.*

And further on...

> *On the other hand, a major and well characterized period of extension developed during the Lias and persisted until Dogger times; on the Cévennes border the extension was oriented E–W to NW–SE (Blès et al., 1989).*

The regional dynamic setting description terminates in page 675:

> *At present, a NNW–SSE compressive horizontal stress still affects parts of the European platform. Present-day stress has not been measured along the Cévennes border but on the basis of observations in nearby regions (Blès and Gros, 1991), a NW–SE stress σ_H (σ_1 or σ_2), can be assumed.*

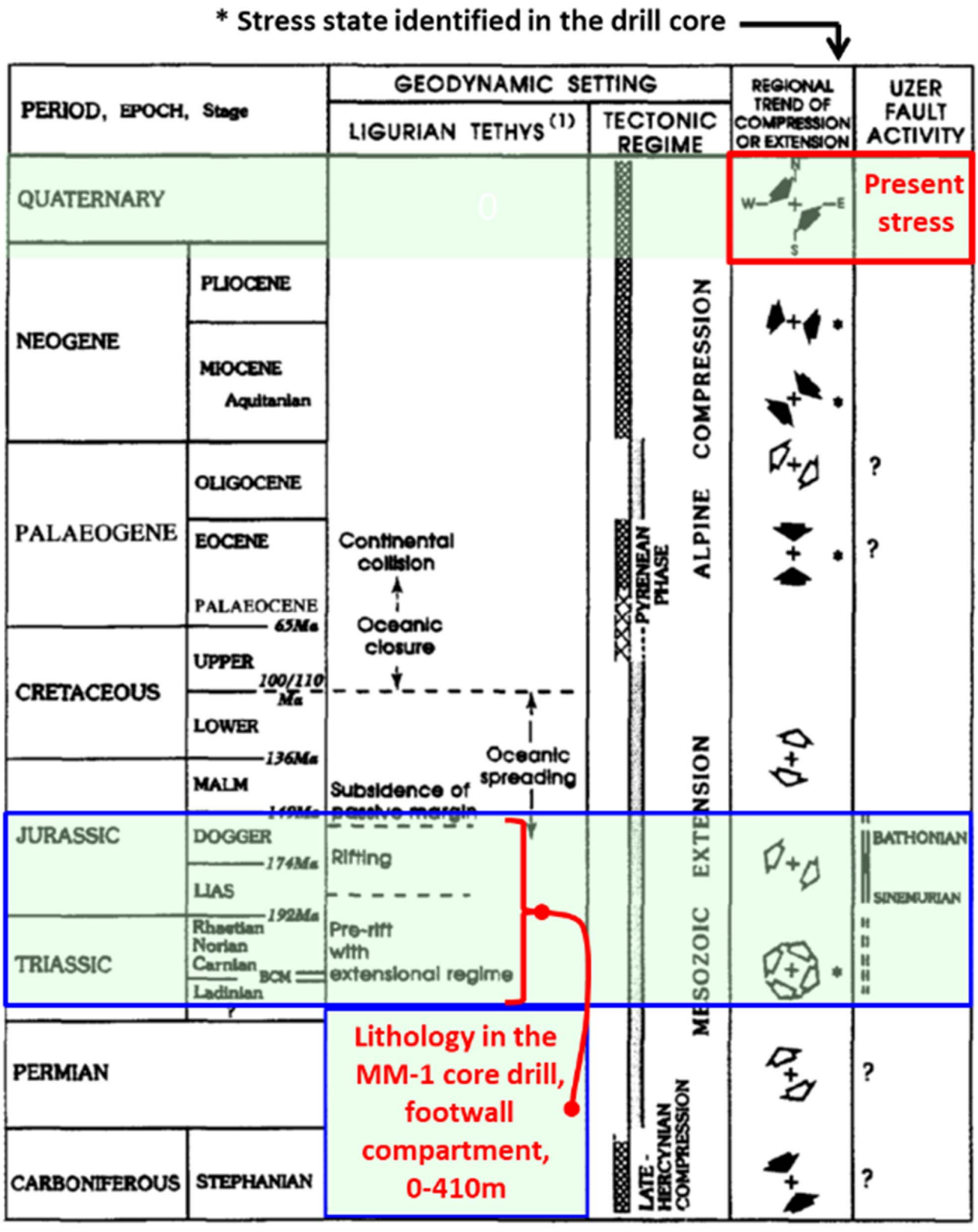

Fig. 23. GPF-Ardèche: Geodynamic setting of the Triassic-Jurassic sedimentary succession of the Cévennes extensional palaeo-margin intersected in the Balazuc BA-1 borehole (this figure modified from *Fig. 3 of Martin and Bergerat* [5]. NOTE: The MM-1 borehole lithology is identical to the BA-1 lithology in the blue box interval.

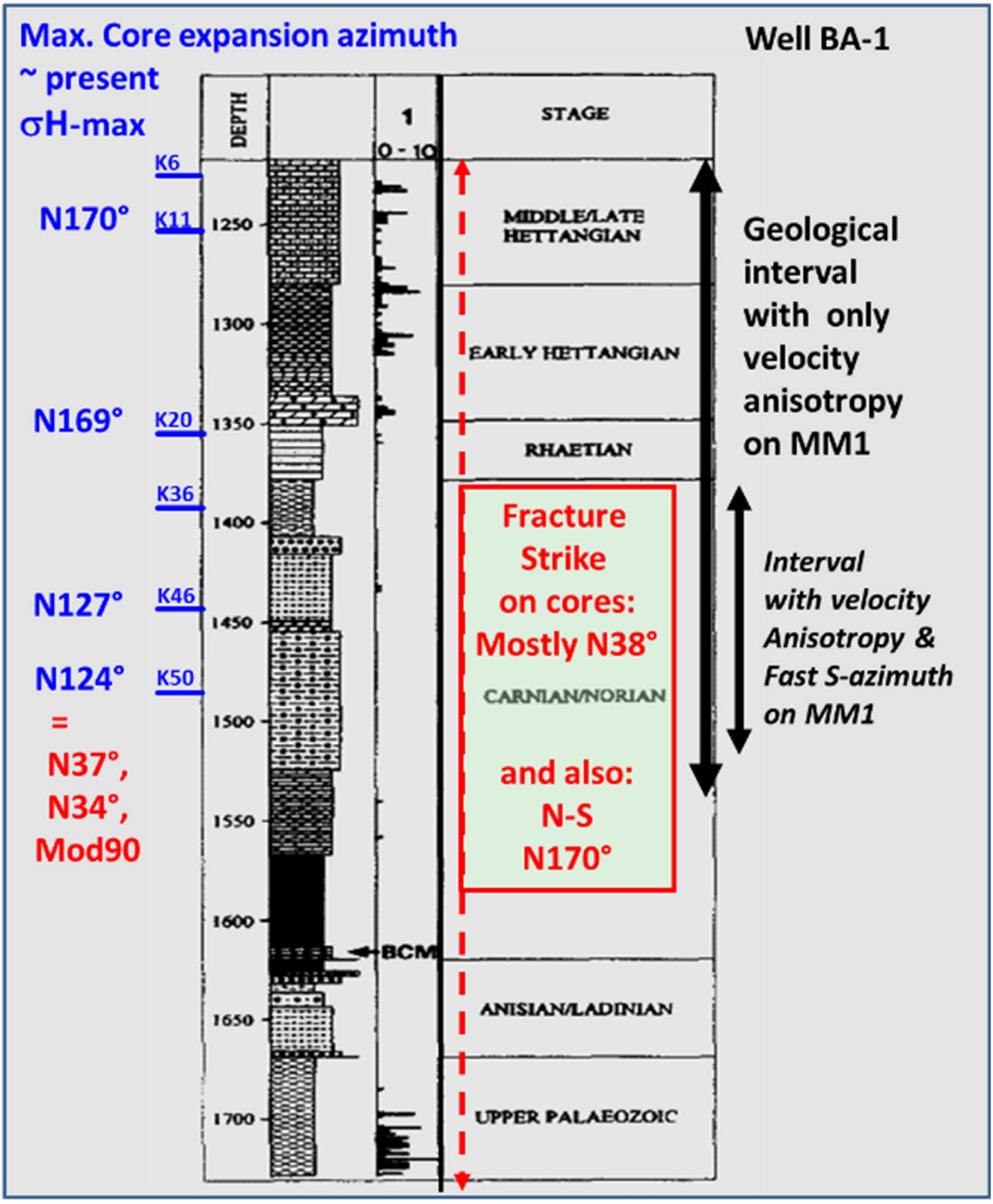

Fig. 24. GPF-Ardèche project: well BA1, modified from *Figure 6 of Martin and Bergerat [5].* Core positions of Anelastic Strain measurements (ASR): K6–K50, yielding present stress results (*Deflandre and Sarda [35]),* to be confronted with palaeo stress directions derived from visual core description of same cores *(from Martin and Bergerat [5])*, and with FMS borehole wall images.

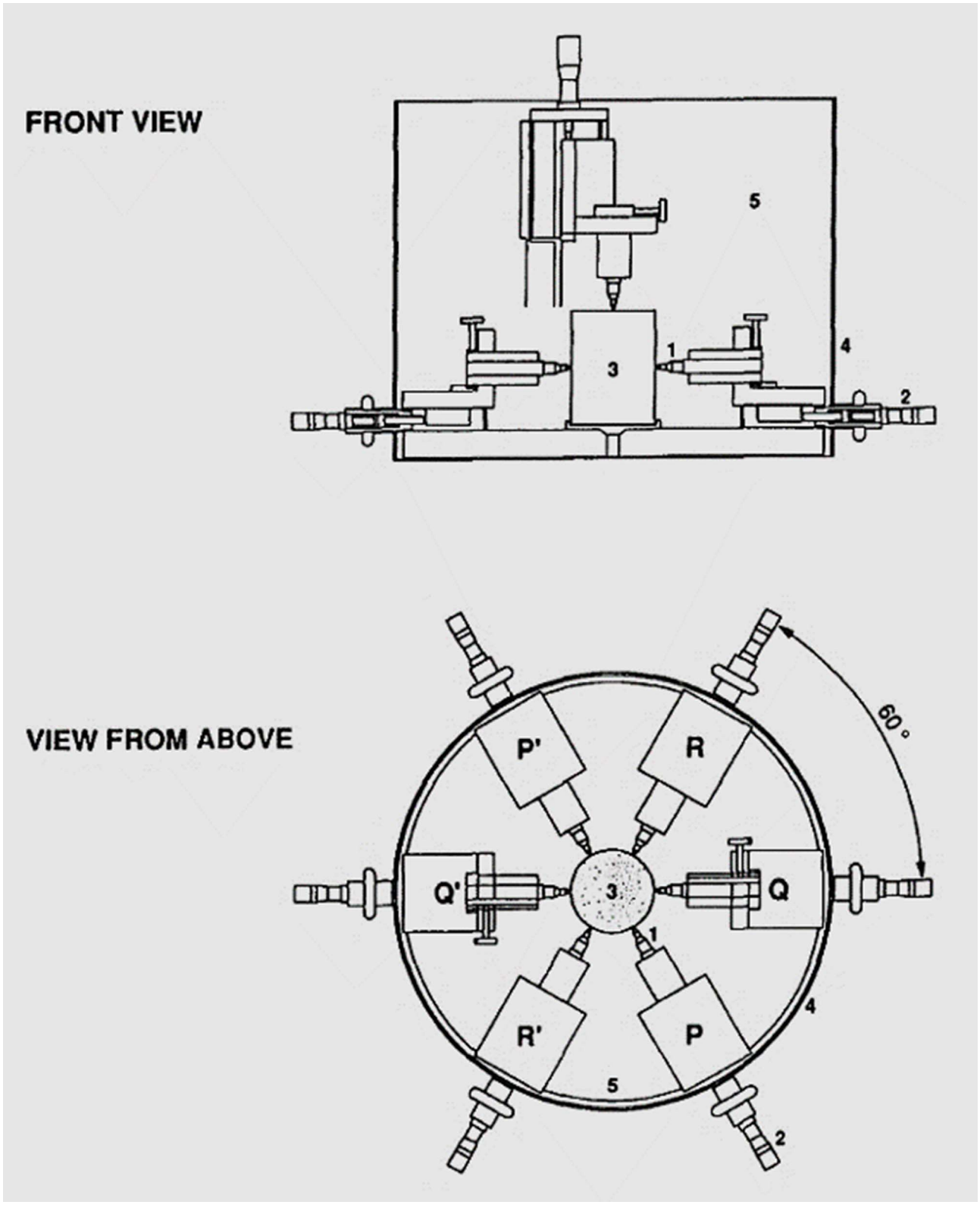

Fig. 25. GPF-Ardèche project: figure reproduced from *Figure 2 of Deflandre and Sarda [35].* Experimental cell for core relaxation measurements, front view and view from above (1: LVDT sensor; 2: micrometer screw; 3: core sample; 4: cell wall; 5: oil).

In summary, the present compressive NW–SE stress in the MM-1 area is illustrated in the red box on the top right side of Figure 23, while the blue box in the lower part of Figure 23 indicates the actual lithology in the shallow depth (0–410 m) of the MM-1 coredrill, accompanied with the continuously oriented NW–SE extensive paleo-stress contemporary of the Uzer fault growth (rightmost track of Fig. 23).

Coincidentally, Figure 24 summarizes the readings of fracture strike on oriented cores (indicated in RED), by *BRGM* geologists Martin and Bergerat [5], and the readings of main core expansion directions (in BLUE, left side), measured on the rig site right after the cores K6–K50 were extracted from the oriented coring barrel, by *IFP* rock mechanic scientists Deflandre and Grard [34], Deflandre and Sarda [35]). If we assume that the direction of large expansion of the core corresponds to the present main horizontal stress direction σ_H along N124°E, it occurs that the present stress direction is nearly orthogonal to the largest N38°E strike population of fractures in the deep Hettangian–Carnian interval of well BA-1, in the same geological interval analyzed on well MM-1 on the upper side of the Uzer fault. Alternatively, if we accept that the present regional direction of main horizontal stress is N170°, the presence of the Uzer fault striking N30° in the close vicinity of the BA-1 and MM1 wells may plausibly locally deviate the main horizontal stress towards N124°... Figure 4 indicates the position of the Anelastic Strain Recovery (ASR) measurements ([34] or [35]) on cores K6–K50 in the deep BA-1 borehole. Figure 25 reproduces the ASR measurement equipment with a plurality of strain LVDT sensors, from *Figure 2 of Deflandre and Grard* [34].

Indeed, the S-wave birefringence response from the MM-1 dipole sonic measurements obtained by D. Belaud and J.P. Yver exhibits a Fast velocity S-wave Azimuth (FAZ) constantly oriented N30°E ± 10° (Figs. 18–21), a direction coherent with the strike of the Uzer fault (Fig. 2) and with the largest population of fractures observed on the BA-1 cores (Fig. 23); *thus the N30°E fast split S-wave azimuth is aligned with the palaeo stress observed on the BA-1 cores (Fig. 23), but nearly at right angle with the present compressive regional stress (Figs. 23 and 24)*; the N30°E azimuth of the fast-Split S-waves measured from the DSI would be expected to predominate in the whole vicinity of the Uzer fault, including both the footwall and hanging wall compartments, a feature to be validated by analyzing the ultrasonic S-wave birefringence on the oriented core samples of both MM-1 and BA-1 for example.

Further multidisciplinary comprehensive studies, including Dipole sonic anisotropy, Shear wave VSP anisotropy, Core analysis and borehole stress measurements are definitely desirable in order to further assess the effective value of the dipole sonic anisotropy results.

Similarly to the stress situation in the Uzer fault vicinity, a correlation between the fast split S-wave azimuth measured in the footwall of a normal fault and the fault strike has been observed in the AIG-10 scientific borehole in Aigio, Greece, from a DSI dataset processed by Prioul *et al.* [36]: the Aig-10 hole intersected the Aigio fault around 770 m, and the footwall interval below this depth is the only interval exhibiting a substantial amount of S-wave birefringence (Fig. 1 of Prioul *et al.* [36], modified in Figs. 5 and 6 of Naville *et al.* [37]), the present stress situation in the Aig-10 well is also complemented by Rousseau [38].

5.6 On the reduction of the Fast Shear wave Azimuth (FSA) errancy and uncertainty output from the DSI data processing routines

Many recent dipole DSI sonic anisotropy surveys have been published, using the Alford–Esmersoy method in geological contexts distant from the Uzer fault one, exhibiting quite more consistent S-wave birefringence Fast Shear-wave Azimuth (FSA) results, with reduced azimuthal uncertainty, mainly where the S-wave velocity magnitude is high: for instance, high S-wave velocity anisotropy (DTS-based anisotropy $> 16\%$) is detected in front of open fractures (Fig. 1 of Prioul *et al.* [39]), while the Min-cross energy is quite NULL, which corresponds to the initial computation hypothesis expressed by Esmersoy *et al.* [10]. In this example [39], the FSA uncertainty range obviously increases where the S-wave velocity anisotropy is weak (DT-based anisotropy $< 4\%$).

The depth intervals isotropic with respect to S-wave velocity might still exhibit differential split S-wave attenuation, unfortunately this parameter is not investigated in the present industrial S-wave birefringence detection process.

Similar observations of Null Minimal cross energy occurs in the nice S-wave birefringence examples published in diverse *Schlumberger* publications [39, 40], therefore the present MM-1 S-wave birefringence result example indicates that it would be appropriate to run an STC/S-wave velocity rotation scan whenever the Min-cross energy is far from being null on the output of the Alford–Esmersoy processing results.

Lastly, when the immediate borehole vicinity is suspected to be heterogeneous, insufficiently symmetrical to the borehole axis (in the cylindrical domain up to three times the borehole radius), the Fast Shear wave Azimuth result might be biased using only a cross-energy minimization approach for the fast S-wave azimuth determination. Sonic investigations in and around the borehole are explained on field cases by oil and gas industrial practitioners in a general overview of the sonic methods using modern field hardware [41].

5.7 On the higher consistency of the Fast Shear wave Azimuth (FSA) detection performed on the depth range restricted to the dipole sonic receiver array by the Rotation-Scan method, illustrated in the present case study

Many researchers investigated the response of a stack of several media with different anisotropy axes, as illustrated for instance by Figures 13 and 14 of Sondergeld and Rai [24], where a stack of two media with different anisotropy azimuthal axes and characteristics is considered: the principal S-wave polarizations received after propagation

in the second medium are INDEPENDENT from the polarization of the incident S-wave train propagated in the first medium of propagation, and independent of the source signal polarization as well.

Accordingly, Figure 22 illustrates a two media situation where the anisotropy axes are possibly different between the dipole emitters and the proximate receiver R1, possibly including a local formation mechanical heterogeneity such a complex fracture surface which may randomly depolarize the S-wave particle motion, as a result of scattering.

The only hypothesis requested to run an STC velocity measurement with is that the depth interval facing the dipole sonic receiver array be fairly homogeneous, as recalled on the right side of Table 1. Of course, in heterogeneous formations, the propagation medium is less likely to have stable anisotropy axes over a long dipole sonic tool spacing (3.5 m distance from source to receiver array) in comparison with the reduced receiver array length (~1 m).

5.8 On the theoretical possibility of encountering non orthogonally polarized S-wave principal modes (paragraph for math – inclined geophysicists)

Dellinger *et al.* [42] expose interesting theoretical development and observations from simulated seismic ray propagation, assessing the possibility of observing NON-ORTHOGONAL polarization of principal S-waves, up to 15° from orthogonality, summarized as follows:

- The eigen shear body waves, or bulk S-waves, and the low frequency eigen flexural S-waves measured by a sonic dipole tool have identical polarization directions.
- The computed propagation model is an orthorhombic anisotropic medium defined by 21 independent coefficients in its symmetric 6 × 6 normalized stiffness matrix, and the presence of a borehole is excluded. The authors observe that *"the medium has almost perfectly longitudinally polarized and transversely polarized shear waves for all propagation directions, but the shear waves are strongly split and (for some group propagation directions) markedly nonorthogonal"*. Along a specific zero-offset ray computed by the authors, the P-wave and split S1, S2 group directions differ by less than 1 degree from the straight line between source and receiver positions, the split S-wave velocity anisotropy being 12% *(legend below Fig. 3 of Dellinger et al. [42]),* and the polarizations of split S-waves remain linear, and oriented in directions differing from the orthogonal by 14.4 degrees (angle called ETA). The authors do not explain if the anisotropy medium considered is induced by cracks, layering, or any other cause.

In the present MM-1 well case study, the differences of FSA (Fast S-wave Azimuth) between the results output from the two S-wave detection methods applied to the same DSI dataset shown in Figures 20, 21a–21c, are indeed much too high to be explained by a propagation in a single, purely homogeneous orthorhombic medium. The MM-1 borehole is vertical, the geological layering is quite horizontal, and the borehole geometry shows negligible ovality.

Additionally, the S-wave anisotropy algorithm called "Rotation scan" can easily cope with the eventuality of non-orthogonal principal Split S-wave detection, as it would be quite easy to refine the STC slowness measurement in a second computer detection run of the Rotation scan routines in directions of reconstructed source polarization ±10 to 20° from the eigen S-wave directions found in the first run… In contrast, the Alford-type algorithm assumes that the split S-waves are orthogonal.

Indeed, *on Figure 5 of Naville [12]*, the Split S-wave detection method developed for downgoing S-wave VSP arrivals was positively tested without difficulty on a field VSP dataset, exhibiting a detection result of non-orthogonal split wave polarizations (60–140 grade or 54°–126°) for the direction of symmetry a double correlation function, leading to 40–160 grade/36°–144° for the split-S-wave polarizations oriented in the orthogonal directions found by the best double correlation result. This old R&D work was aimed to explore the S-wave propagation properties for the definition of Split S-wave methods to be developed for converted P-S, and S-S surface reflection surveys carried out by GGG…

Interestingly, the paper by Sun and Prioul [43], "*Relating shear sonic anisotropy directions to stress in deviated wells*", deals with orthorhombically stressed and anisotropic propagation medium often encountered in deviated wells, and focuses mainly on the detection of the Fast Shear wave Azimuth (FSA) from the dipole sonic anisotropy processing routines. The possible non-orthogonality of eigen split S-waves is not mentioned.

5.9 On the operational dipole sonic applications, in open hole and cased hole?

Traditionally the wireline sonic log is run in open hole conditions, because it is often quite difficult to obtain correct P-wave velocity *Vp* in a well cemented cased hole. In poorly cemented cased hole, P-wave propagation in the casing pipe is prevalent and large amplitudes of P-wave casing arrivals mask the P-wave formation arrivals.

In contrast, dipole sonic tools operated in cemented cased hole yield excellent S-S reflection results, regularly up to 40 m laterally to the well, as reported with dipole sonic tool of various service companies and sonic seismic signal processors: for instance, similar S-reflection results have been obtained in the SAME hole before and after casing installation, by Tang *et al.* [44], and clear S-S wave reflection results in the open hole were obtained by Lee *et al.* [45] and by Wielemaker *et al.* [46]. Of course, P-P reflections may not originate from the same reflectors as S-S reflections, however the S-S dipole sonic reflected signals do not suffer any interference with undesired Stoneley waves propagating along the borehole, in contrast with P-P reflections recorded by monopole source and receivers.

Therefore, one would expect that the S-wave birefringence parameters can be extracted from the direct dipole sonic flexural S-waves in cemented cased hole.

5.10 On the low values of velocity anisotropy intervals

The anisotropy results obtained by the STC-Rotation Scan method (Figs. 20, 21a–21c) show that the independently

determined slow S-wave azimuth is more erratic than the Fast S-wave Azimuth (FAZ), and not always orthogonal to FAZ when the velocity anisotropy is small: it could mean that the slow S-wave is more attenuated than the fast S-wave, not only where velocity anisotropy is present, unfortunately the attenuations of the split S-waves have not been computed to confirm this conjecture.

Surprisingly, the stable N30°E FAZ found in nearly isotropic intervals should indeed be indetermined, and the N30°E FAZ orientation stability can be observed even where the DSI tool rotates in the low anisotropy depth intervals (The DSI tool orientation is the blue curve in Track 2 of Figs. 20, 21a–21c).

Although the low values of velocity anisotropy (<4%) determined from the Rotation-Scan method in the MM-1 study cannot be fully assessed as physically significant, the consistency of the FAZ/fast S-wave azimuth direction is noteworthy and constitutes a good indicator of reliability from the geologist point of view; the latter observation made on a single well at rather shallow depth definitely calls for a larger investigation from many more dipole sonic surveys collected in various geologic contexts.

In order to evaluate the efficiency of the STC rotation scan computation efficiency to separate two near orthogonal linearly polarized split S-waves with SAME velocity, but DIFFERENT attenuations, one should apply first the SAME geometrical spreading compensation on amplitudes of X and Y signals recorded from any emission (and avoid single component amplitude normalization at preprocessing stage). Personal estimation of the semblance from same velocity S-waves with an amplitude difference of a factor 2 (6 db) over the DSI receiver array seems to be necessary to obtain a significant gradient of the semblance parameter for split S-wave separation. Such differential attenuation (6 db or more) between split S-waves would occur mainly where open fractures are present facing the DSI receiver array; this subject would need further studies on synthetic seismic data, then on field data, over borehole depth intervals with open fractures and with tight fractures, in order to collect realistic estimates of non-dispersive sonic flexural S-wave attenuation over the typical 1 m long receiver array of many commercial dipole sonic tools.

6 Further related readings about of S-wave birefringence

After a limited scouting of the existing publications as of 2021, the authors deliver here a brief overview over the specific subject of shear wave splitting, how it works and what it means; a short list of significant publications is mentioned below in order to attract the attention of the interested reader, as follows:

- In his 1998 paper entitled "Shear-wave splitting in a critical crust: the next step" [47], S. Crampin produced an easy-reading summary on the state knowledge about S-wave birefringence, (ref: Proceedings of the The Eighth International Workshop on Seismic Anisotropy; 8IWSA).
- In the 2006 "Review of techniques for measuring birefringence above small earthquakes" [48], the seismologist authors S. Crampin and Y. Gao explain the "*Reasons why shear-wave splitting above small earthquakes are difficult to measure*", in Table 1, and express the "*Common fallacies in measuring and interpreting shear-wave splitting",* in Table 2.
- In 2017, the seismologist authors Z. Li and Z. Peng summarize "*Stress- and structure-induced anisotropy in Southern California from two decades of shear wave splitting measurements*" [49], from a sizable amount of 232,000 SWS measurements. In their introduction, they note that: "*... remnant features of paleostress ... can also cause crustal anisotropy... Anisotropy associated with faults... is generally categorized as structure-induced anisotropy".* These documented statements from redundant Californian observations could certainly help interpreting the birefringence observations made in the *BRGM* MM-1 borehole from DSI measurements, to be confronted with paleostress core description, in the immediate vicinity of the major Uzer normal fault.
- In 1996, RR. Kendall and JM. Kendall indicate that "*Amoco has acquired, processed and interpreted the pure Shear-wave components of four 9-component seismic lines (2D-9C) in south-central Wyoming, as well as crossed-dipole sonic logs* (using the SLB-DSI tool), *and 9C VSP's* [50]. Additional oriented cores were taken from the wells and their fractures were described. Interestingly, *Figure 3 of paper [50]* shows the classical DSI display of the birefringence processing results and exhibits a Fast S-wave azimuthal scattering similar to the one produced in MM-1 (Figs. 17a, 17b or 19 of the present paper), although with a lower amounts of S-wave velocity anisotropy. Curiously, the authors do not comment on the large discrepancies between the observed Slowness-based velocity Anisotropy (SLOANI) and Time-based Anisotropy (TIMANI) percent values.
- In 1997, B.W. Tichelaar and P.J. Hatchell presented detailed results from in-house processing of a DSI dataset [51], accompanied with a solid discussion about the influence of the hole ovality and the relative contrast between flexural S-wave velocity and Stoneley/tube wave velocity on the azimuth of the fast S-wave and on the percent amount of observed S-wave velocity anisotropy computed. The whole anisotropy detection procedure from 4C borehole flexural waves have been revised by the authors. The example of a typical 4-Component/7 receiver level DSI raw record cycle is shown the *Appendix Figure A-4 [51].* The same 2 × 2 matrix signal response is displayed after inversion and best diagonalization on the *Appendix Figure A-3 [51]*, with TRUE relative amplitude of the 28 trace signals, and has been reproduced in Figures 26a and 26b of the present paper, on which colored time lines joining the signal zero crossings have been drawn (red for the Fast eigen S-wave, blue for the Slow S-wave): the depth of this 4-C data cycle sample shows a definite S-wave velocity anisotropy, about 10%, and probably

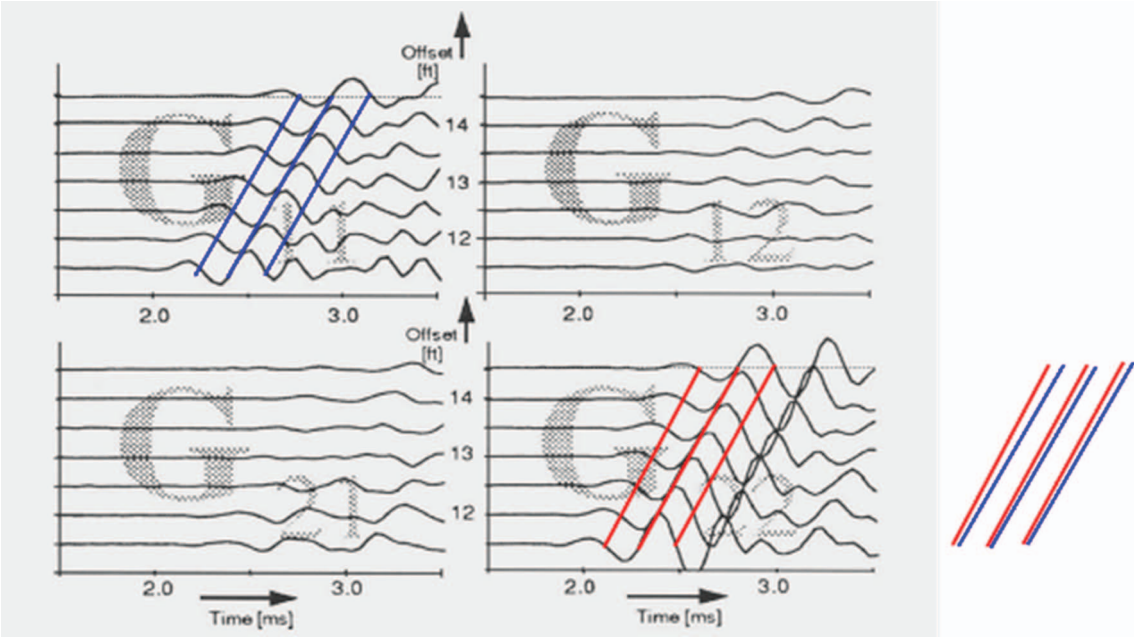

Fig. 26a. Reproduced and modified from *Figure A-3 of Tichelaar and Hatchell [51]*: *The four components of the propagator matrix G diagonalized in eigen S-wave coordinates, over the 7 DSI computation receiver levels.* The principal S-wave waveforms on the diagonal clearly show differing S-wave velocities, the eigen waveform G_{22} (red) being faster than G_{11} (blue). Time lines are superposed on the right side.

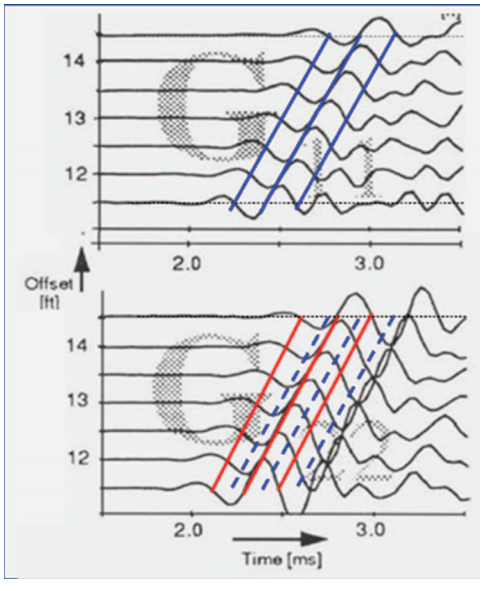

Fig. 26b. Eigen Diagonal FAST Shear waveform G_{22} (red) clearly exhibits nearly TWICE higher amplitudes than the SLOW Shear waveform G_{11} (solid blue line, copied as dashed lines on G_{22}). Interestingly, the eigen waveforms G_{22} and G_{22} look very much alike on the first two peaks, after which they shape DIFFER, a major third peak present only on G_{22}, in spite of the SIMILAR shape of the source pulses emitted by the two orthogonal transmitters mounted on the DSI dipole sonic tool. The energy of the two source transmitters has been equalized after filtering out the DC offset at preprocessing stage, before 4C inversion and diagonalisation of the recorded flexural wave signals.

corresponds to the Upper Natih interval affected by a large hole ovality: it is noteworthy to observe that the principal waveforms G_{11} and G_{22} signals are identical ONLY on the first two peaks of the signal, in spite of the similar source signal emitted by the two orthogonal DSI transmitters, which could mean that the signal actually imparted by the pressure transmitters into the rock formation depends on the borehole ovality. Actually, the S-wave response recorded by the DSI receivers is shown to be dependent on the borehole ovality. The S/N ratio of the DSI signals is excellent; the little S-wave energy residuals remaining on the off-diagonal elements mean that the rock formation may not be fully homogeneous between the source transmitters and the array of receivers. In addition, the fast principal flexural S-wave G_{22} visibly has higher amplitudes than the Slow flexural S-wave G_{11}. Indeed, we cannot even conclude that this amplitude contrast can be attributed to the propagation attenuation in the rock formation in the interval between the source position to the proximate receiver position, as the borehole section shown by the 4 arm caliper log is locally oval. In contrast, measuring the flexural S-wave attenuation over the receiver array interval should be more reliable, as long as the borehole geometry is consistent in the restricted 1 m array length... Further insights, comments, discussion about S-wave birefringence results from VSP, dipole sonic and 9C-3D surface seismic survey can be found in papers by Hake *et al.* [52], and by production geoscientists Hitchings and Potters [53], although the subject of S-wave attenuation had not been considered.

7 Way forward

Since the dipole sonic data and the oriented cores still exist in the *BRGM* archives and storage, several additional actions can be outlined and effectively performed:

- Orientation of the existing MM-1 cores with help of the FMS images, followed by a detailed description of the core fractures, similarly to what was done on BA-1 cores by Martin and Bergerat [5]. Azimuth of preferred permeability will be tentatively assessed where the MM-1 borehole crossed permeable fractures.
- Measuring the birefringence on a series of undamaged MM-1 oriented core samples at ultrasonic frequencies in the lab, in order to calibrate the birefringence results obtained from the DSI methods, at least where undamaged cores are recovered. Same on the cores K6–K50 extracted from the BA-1 well, for which the ARS core expansion was measured on the drilling site, in order to confront the ASR and birefringence results.
- Reprocessing the DSI data on MM-1, in order to better understand the flexural S-wave generation and propagation and improve the birefringence detection method and reliability in ancient, tight geological formations similar to the ones encountered in SE France.
- Implementing the processing route to determine the split S-wave intrinsic attenuations and the differential Split S-wave attenuation (a parameter independent from geometrical spreading), notably in the highly anisotropic fractured intervals where the cores are naturally fractured and where the dipole sonic data are the only ones able to quantify the S-wave birefringence. Anisotropy of velocity and attenuation should be looked as equally important S-wave anisotropy attributes.
- Refining the birefringence interpretation with results from all the above specialists involved by and for the geologist end-user.

Recognizing and evaluating the heterogeneity of rock mechanical parameters in the immediate borehole vicinity, and depending on the geological context, may lead to further developments in the practice of industrial S-wave birefringence detection methods from dipole sonic measurements: several dipole sonic data processing methods might need to be routinely applied to improve the petrophysical and mechanical characterization of the near borehole formation.

The velocity and attenuation anisotropy attributes derived from dipole sonic measurements are expected to help the reservoir engineer distinguishing between the open, potentially permeable fractures from the tight ones, as a complement to the borehole wall images.

Lastly, it would seem appropriate for the academic and industrial practitioners to update a detailed review of signal processing techniques for estimating the birefringence attributes more thoroughly, as Macbeth and Crampin have undertaken in the early 1990's [54], taking in account the most recent S-wave detection experiments and methods, sorting velocity and attenuation logs in all wave modes, as shown for instance by Che and his colleagues in their case study paper relating to Tatarstan carbonates, using a modern multimode full waveform sonic tool [55].

Further S-wave splitting detection improvements might arise using borehole arrays of 3C seismic sensors to record earthquakes where the local horizontal stress is suspected to vary with time, as observed by Crampin [56]. Numerous boreholes abandoned by the oil and gas and mining industry could be convenient to this purpose, before definite plugging.

8 Conclusion

The present experimental study conducted in the *BRGM* MM-1 well is very promising for an improved characterization of open fractures, potentially permeable, exhibiting high S-wave velocity anisotropy magnitude, while the anisotropy of the tight/cemented fracture intervals is identical to the rock matrix anisotropy.

The shallow 300 m interval of the MM-1 coredrill presents no abnormal borehole geometry features susceptible to disturb the dipole sonic measurements, except for the presence of local open permeable fractures. The measurement conditions with the oriented DSI-GPIT-GR tool combination present no technical anomaly. A repeat run had been recorded.

The discrepancies between the fast S-wave anisotropy azimuth/FSA resulting from the two different detection processing procedures exposed in the present study are still not fully explained; however, the heterogeneity of mechanical formation parameters within a short radius around the borehole, and the ruggedness of the borehole wall are suspected to alter the symmetry of the propagation medium around the well axis, which can randomly change the polarization of the emitted S-wave propagated between the source position and the closest DSI array receiver, as summarized in Table 1. The simple azimuthal rotation scan of S-wave velocity determination using the standard STC routine seems to yield the most accurate results, with higher depth resolution along the well trajectory, and higher accuracy for the fast S-wave azimuth: these features are more reasonably credible for the geologist.

The N30°E fast split S-wave azimuth is mainly aligned with the paleo stress observed on the BA-1 cores (Fig. 23), nearly at right angle with the present compressive regional stress N124° or N170°E, indicated by diverse authors: Figures 1 and 2 illustrate the "stainless glass" aspect of the regional fault pattern around the MM-1/BA-1 drilling site. Unfortunately, no direct measurements of the present stress were conducted in the MM-1 well, and the MM-1 cores have not been examined with as much attention as the BA-1 ones.

The erratic azimuthal results of the Alford–Esmersoy procedure applied in the present experimental DSI survey look abnormal to the geologists and call for further investigation and understanding, on similar case studies. If physically true, such principal S-wave azimuthal errancy would make it very difficult to upscale the Shear wave splitting formation response into thick equivalent anisotropic layers of sedimentary formations or crustal layers. The capacities

of present-day computers should allow to routinely run several anisotropy detection methods, including on the drill site as desired.

Acronyms

BRGM	Bureau de recherches géologiques et minières (French Geological Survey)
DSI	Dipole Shear Imager
GPIT	General Purpose Inclinometer Tool
AMS	Auxiliary Measurements
NGS	Neutron-induced Gamma Ray Spectroscopy
DLL	Dual LateroLog
LDT	Litho-Density Tool
CNL	Compensated Neutron Log
FMS	Formation Micro Scanner
V_p, V_s, respectively	P-wave, S-wave velocity; velocity = 1/slowness
FSA	Fast S-wave Azimuth
STC	Slowness Time Coherence; method for measuring a wave slowness (DT) from an array sonic tool dataset, using the computation of the semblance function
DT, DTfast, DTslow, respectively	Transit time (μs/ft), Fast-S transit time, Slow S-transit time. DTCO = DT-Pwave, DTSmin = DTfast, DTSmax = DTslow.
Array-ANI, $\Delta V/V$, or SLOANI	Shear Slowness Anisotropy computer from STC slownesses over the receiver array of the DSI tool: SLOANI = 2 (DTslow − DTfast)/(DTslow + DTfast)
T-R ANI or TIMANI	Time-based shear anisotropy = relative difference of the flexural arrival at mid-receiver array location
ASR	Anelastic Strain Recovery
SWS	Shear Wave Splitting
SLB	Schlumberger
VSP	Vertical Seismic Profile

Acknowledgments. Many professionals of different disciplines contributed to the present scientific project. The DSI survey in the MM-1 coredrill was decided as an extra field effort by *BRGM* and *Schlumberger* in the early 1990's, on *IFP*'s suggestion. The DSI anisotropy processing process had to be invented and refined at the time and was carried out as an experimental task by *Schlumberger-France*. The surface seismic image had been graciously refined post drilling by *CGG-France*, integrating borehole VSP and sonic log data into an early depth migration procedure by Alain Mignot and Serge Zimine. Michel Degouy of *BRGM* was the on-site drilling manager-geologist, and accommodated the collection of numerous borehole data whenever possible, including operating downhole explosive charges in the open hole, as a downhole reverse VSP/walkaway source test, followed by a successful borehole cleanup from all residual debris. The principle of an azimuthal scan of shear wave velocity measurement applied by the co-authors, here coined "DTS azimuthal rotation scan", was inspired by the approach of S-wave time-picking azimuthal scan applied to S-wave VSP datasets recorded by two orthogonal horizontal surface sources, initiated by Leonid Y. Brodov and his colleagues of VNII-Geofizika, Moscow, in the late 1980's. The authors appreciate the technical exchanges over the present paper with Jean-Luc Mari, Jean-Claude Lecomte, and Jean-Pierre Deflandre, respectively geologist, geophysicist and rock mechanics engineer with *IFPEN*, and the remarks of the anonymous reviewers. Special thanks to the past managers of *IFP* and *BRGM* who agreed to perform innovative field measurements with the newly built DSI tool in the early 1990's, and to the present managers of both institutions who agreed to publish the results. Last, the technical exchanges held in 1992 with *ELF-Aquitaine*, *TOTAL*, *Gaz De France (GDF)* and *IFPEN* with *Franck Morris*, who designed the Dipole DSI tool in *Schlumberger-Japan*, were quite helpful in understanding the technology and characteristics of the DSI tool, which incited the industrial operators to test the dipole sonic tool for reservoir formation characterization.

References

1 Bonijoly D., Sureau J.F., Steinberg M. (1996) GPF Ardèche: A scientific drilling programme for fluid-rock interaction studies along an extensional Paleo-margin, *Mar. Pet. Geol.* **13**, 6, 605–606. https://doi.org/10.1016/0264-8172(96)82615-8.

2 Giot D., Roure F., Elmi S., Lajat D., Steinberg M. (1991) The discovery of major extensional faults of Jurassic age on the continental margin of the Southeast Basin, Ardèche, France (GPF program), *CR Acad. Sci. Paris* **312-II**, 747–754.

3 Giot D., Roure F., Dromart G., Elmi S., Naville C., Perrin J., Steinberg M. (1991) Dynamics of a passive Jurassic margin: the main phases in the activity of the Uzer fault as revealed by Balazuc drill hole 1, Ardèche, France, *CR Acad. Sci. Paris* **313-II**, 1463–1469.

4 Bonijoly D., Perrin J., Roure F., Bergerat F., Courel L., Elmi S., Mignot A., the GPF Team (1996) The Ardèche paleomargin of the South-East Basin of France: Mesozoic evolution of a part of the Tethyan continental margin (Géologie Profonde de la France programme), *Mar. Pet. Geol.* **13**, 6, 607–623. https://doi.org/10.1016/0264-8172(95)00075-5.

5 Martin P., Bergerat F. (1996) Palaeo-stresses inferred from macro- and microfractures in the Balazuc-1 borehole (GPF programme). Contribution to the tectonic evolution of the Cévennes border of the SE Basin of France, *Mar. Pet. Geol.* **13**, 6, 671–684.

6 Gratacos B., Bale R., Granger P.Y. (2009) Amplitude effects associated with shear wave splitting, in: *SEG Technical Program Expanded Abstracts*, pp. 4284–4288. https://doi.org/10.1190/1.3255779.

7 Naville C. (1988) Method of measuring the anisotropy of propagation or reflection of a transverse wave, particularly a method of geophysical prospecting by measurement of the anisotropy of propagation or reflection of shear waves in rocks. *US Patent 4,789,969.*

8 Far M.E., Liu E., Downton J. (2015) Introduction to special section: fractures. SEG Library, *Interpretation* **3**, 3, 1A–T181. https://library.seg.org/doi/epub/10.1190/INT2015-0611-SPSEINTRO.1. https://www.researchgate.net/publication/282462777_Introduction_to_special_section_Fractures.

9 Belaud D., Standen E. (1995) Fracture using Shear anisotropy and electric images, in: *3rd International Symposium on Geotomography-Fracture imaging, November 8–10, Tokyo.*

10 Esmersoy C., Koster K., Williams M., Boyd A., Kane M. (1994) Dipole shear anisotropy logging, in: *60th Annual Meeting, SEG, 1994, Expanded abstracts, Paper SL3.7.*

11 Alford R.M. (1986) Shear data in presence of azimuthal anisotropy, in: *56th Annual Meeting*, SEG, Expanded abstracts, pp. 476–479.

12 Naville C. (1986) Detection of anisotropy using shear wave splitting 1986 in VSP surveys: Requirements and applications, in: *56th Annual Meeting*, SEG, Expanded abstracts S5.2, pp. 391–394.

13 Kimball C., Marzetta T. (1984) Semblance processing of borehole acoustic array data, *Geophysics* **49**, 272–281.

14 Bouchon M., Schmitt D.P. (1989) Full wave logging in an irregular borehole, *Geophysics* **54**, 758–765. https://doi.org/10.1190/1.1442618.

15 Coppens F., Mari J.L. (1995) Application of the intercept time method to full waveform acoustic data, *First Break* **13**, 1.

16 Hornby B. (1993) Tomographic reconstruction of near-borehole slowness using refracted borehole sonic arrivals, *Geophysics* **58**, 12, 1726–1738. https://doi.org/10.1190/1.1443387.

17 Tang X., Xu S., Zhuang C., Chen X. (2016) Quantitative evaluation of rock brittleness and fracability based on elastic-wave velocity variation around borehole, *Pet. Explor. Dev.* **43**, 3, 457–464. https://doi.org/10.1016/S1876-3804(16)30053-2.

18 Plona T., Sinha B., Kane M., Shenoy R., Bose S., Walsh J., Endo T., Ikegami T. (2002) Mechanical damage detection and anisotropy evaluation using dipole sonic dispersion analysis, in: *Paper presented at the SPWLA 43rd Annual Logging Symposium, Oiso, Japan, 2–5 June 2002.*

19 Su Y., Zhen L., Xu S., Zhuang C., Tang X. (2018) Elastic-wave evaluation of downhole hydraulic fracturing: Modeling and field applications, *Geophysics* **83**, 1, 1JF-Z3. https://doi.org/10.1190/geo2017-0054.1.

20 Tang X., Chunduru R.K. (1999) Simultaneous inversion of formation shear-wave anisotropy parameters from cross-dipole acoustic-array waveform data, *Geophysics* **64**, 5, 1502–1511. https://doi.org/10.1190/1.1444654.

21 Market J., Mejia C., Mutlu O., Shahri M.P., Tudge J. (2015) Untangling acoustic anisotropy, in: *Paper presented at the SPWLA 56th Annual Logging Symposium, Long Beach, California, USA, July 2015.*

22 Hornby B.E., Howie J.M., Ince D.W. (1999) Anisotropy correction for deviated well sonic logs: Application to seismic well tie, in: *65th Annual Meeting*, SEG. Expanded Abstracts. https://doi.org/10.1190/1.1820700.

23 Blanch J.O., Cheng A.C.H., Varsamis G.L. (2002) A method to extract fast and slow shear wave velocities in an anisotropic formation, in: *SEG Expanded Abstracts*, pp. 352–355. https://doi.org/10.1190/1.1817251.

24 Sondergeld C.H., Rai C.S. (1992) Laboratory observations of shear-wave propagation in anisotropic media, *The Leading Edge of Exploration* **11**, 2,38–43.

25 Zhuang C., Xu S., Li H., Su Y., Tang X. (2019) Azimuthal shear-wave anisotropy measurement in a borehole: Physical modelling and dipole acoustic verification, *JASA* **146**, EL129. https://doi.org/10.1121/1.5120551.

26 Kessler C., Varsamis G.L. (2001) A new generation crossed dipole logging tool: design and case histories, in: *SPE 71740, 2001, SPE Annual Conference, New Orleans, Louisiana.*

27 Humbert F., Louis L., Barnes C., Robion P., David C., Song S.R. (2012) Lithological control on shear-wave velocity anisotropy in core samples from the Taiwan Chelungpu Fault Drilling Project, *J. Asian Earth Sci.* 63–72. https://doi.org/10.1016/j.jseaes.2012.02.012.

28 Hung J.-H., Ma K.-F., Wang C.-Y., Ito H., Lin W., Yeh E.-C. (2009) Subsurface structure, physical properties, fault-zone characteristics and stress state in scientific drill holes of Taiwan Chelungpu Fault Drilling Project, *Techtonophysics* **466**, 307–321. https://doi.org/10.1016/j.tecto.2007.11.014.

29 Morris C.F., Little T.M., Letton W. (1984) A new sonic array tool for full waveform logging, in: *Paper Number: SPE-13285-MS, SPE Annual Conference, Houston, Texas, September 1984.* https://doi.org/10.2118/13285-MS.

30 Brie A., Endo T., Hoyle D., Codazzi D., Esmersoy C., Hsu K. (1998) New directions in sonic logging, *Oilfield Rev.* **10**, 40–55. Schlumberger. https://www.academia.edu/23890995/DSI_Logging_Applications. https://docplayer.net/10128122-New-directions-in-sonic-logging.html.

31 Close D., Cho D., Horn F., Edmundson H. (2009) The sound of sonic: a historical perspective and introduction to acoustic logging, *CSEG Record.* **34**, 05. https://csegrecorder.com/articles/view/the-sound-of-sonic-a-historical-perspective-and-intro-to-acoustic-logging.

32 Donald J.A., Wielemaker E.J., Karpfinger F., Liang X., Tingay M. (2015) Qualifying stress direction from borehole shear sonic anisotropy, in: *49th U.S. Rock Mechanics/Geomechanics Symposium, San Francisco, California, June 2015. ARMA-2015-364.*

33 Tang X. (2017) Advances in borehole acoustic reflection imaging, *ASA Proc. Mtgs. Acoust.* **32**, 032001. https://doi.org/10.1121/2.0000705.

34 Deflandre J.P., Grard G. (1992) Anelastic strain recovery measurements on the site of Balazuc "Géologie Profonde de la France" Program, in Documents du BRGM, n°223, in: *VIth International Symposium. Continental Scientific Drilling Programs, Paris, April 1992.*

35 Deflandre J.P., Sarda J.P. (1992) Core relaxation measurements on compacted sedimentary formations (well Ba 1), in: *Proc 33rd US Symposium on Rock Mechanics, Santa Fe, 3–5 June 1992*, Publ Rotterdam: A A Balkema, pp. 49–57. ISBN 90 5410 0451.

36 Prioul R., Plona T., Kane M., Sinha B., Kaufman P., Signer C. (2004) Azimuthal anisotropy using shear sonic imager: Insights from the AIG 10 well, Corinth Rift Laboratory [Anisotropie azimutale par diagraphie sonique des ondes de cisaillement: données du forage AIG 10, laboratoire du rift de Corinthe], *CR Geosci.* **336**, 477–485. https://doi.org/10.1016/j.crte.2003.11.008. https://www.sciencedirect.com/science/article/pii/S1631071304000173.

37 Naville C., Cuenot N., Tselentis A., Kazemi K., Serbutoviez S., Bruneau J. (2021) S-wave birefringence variations from stress, pore pressure? in: *55th US Rock Mechanics/Geomechanics Symposium, Houston, Virtual, June 2021, ARMA 21-A-1794.* https://onepetro.org/ARMAUSRMS/proceedings-abstract/ARMA21/All-ARMA21/ARMA-2021-1794/468253.

38 Rousseau A. (2006) *Model of horizontal stress in the Aigion10 well (Corinth) calculated from acoustic body waves.* https://hal.archives-ouvertes.fr/hal-00018406/document

39 Prioul R., Donald A., Koepsell R., El Marzouki Z., Bratton T. (2007) Forward modeling of fracture-induced sonic anisotropy using a combination of borehole image and sonic logs, *Geophysics* **72**, 4, E135–E147. https://doi.org/10.1190/1.2734546.

40 Donald A., Bratton T. (2006) Advancements in acoustic techniques for evaluating natural fractures, in: *SPWLA 47th Annual Logging Symposium, Veracruz, Mexico, June 4–7, 2006*.

41 Arroyo Franco J.L., Mercado Ortiz M.A., De G.S., Renlie L., Williams S. (2006) Sonic investigations in and around the borehole, *Oilfield Rev.* 14–33. Schlumberger. https://www.researchgate.net/publication/289978814_Sonic_investigations_in_and_around_the_borehole.

42 Dellinger J.A., Nolte B., Etgen J.T. (2001) Alford rotation, ray theory, and crossed-dipole geometry, *Geophysics* **66**, 2, 637–647.

43 Sun H., Prioul R. (2010) Relating shear sonic anisotropy directions to stress in deviated wells, *Geophysics* **75**, 5, D57–D67.

44 Tang X.M., Gu X.H., Lee S.Q. (2020) Borehole acoustic reflection imaging through casing: theory and application, in: *82nd EAGE Annual Meeting, Expanded Abstracts Fr_P05_08, December 2020*.

45 Lee S.Q., Chen M., Gu X.H., Su Y.D., Tang X.M. (2019) Application of four-component dipole shear reflection imaging to interpret the geological structure around a deviated well, *Appl. Geophys.* **16**, 291–301. https://doi.org/10.1007/s11770-019-0778-x.

46 Wielemaker E., Cavalleri C., Dahlhaus L., Reynaldos A., Sosio G., Ungemach P., Antics M., Davaux M. (2020) Delineating the geothermal structure and flow properties in a sub-horizontal well with the use of wireline and LWD data in a multiphysics approach, in: *2020 SPWLA 61st Annual Online Symposium, June 22, 2020*. https://doi.org/10.30632/SPWLA-5065.

47 Crampin S. (1998) Shear-wave splitting in a critical crust: the next step. *Oil Gas Sci. Technol – Rev. IFP* **53**, 5, 749–763. Proceedings of the Eighth International Workshop on Seismic Anisotropy (81WSA), 20–24 April 1998. https://hal.archives-ouvertes.fr/hal-02079026/document. https://ogst.ifpenergiesnouvelles.fr/articles/ogst/pdf/1998/05/crampin_v53n5.pdf

48 Crampin S., Gao Y. (2006) A review of techniques for measuring shear-wave splitting above small earthquakes, *Phys. Earth Planet. Inter.* **159**, 1–2, 1–14. https://www.sciencedirect.com/science/article/pii/S0031920106001853.

49 Li Z., Peng Z. (2017) Stress- and structure-induced anisotropy in Southern California from two decades of shear wave splitting measurements, *Geophys. Res Lett.* **44**, 9607–9614. https://doi.org/10.1002/2017GL075163.

50 Kendall R.R., Kendall J.M. (1996) Shear-wave amplitude anomalies in south-central Wyoming, *The Leading Edge* **15**, 8, 913–920. https://doi.org/10.1190/1.1437390.

51 Tichelaar B.W., Hatchell P.J. (1997) Inversion of 4-C borehole flexural waves to determine anisotropy in a fractured carbonate reservoir, *Geophysics* **62**, 5, 1432. https://doi.org/10.1190/1.1444247.

52 Hake J.H., Gevers E.C.A., Van Der Kolk C.M., Tichelaar B.W. (1998) A shear experiment over the Natih field in Oman: pilot seismic and borehole data, *Geophys. Prospect.* **46**, 617–646. https://doi.org/10.1046/j.1365-2478.1998.00111.x.

53 Hitchings V.H., Potters H. (2000) Production and Geological implications of the Natih 9C3D Seismic Survey, *GeoArabia* **5**, 4, 511–524. https://doi.org/10.2113/geoarabia0504511.

54 Macbeth C., Crampin S. (1991) Comparison of signal processing techniques for estimating the effects of Anisotropy, *Geophys. Prospect.* **39**, 3, 357–385. https://doi.org/10.1111/j.1365-2478.1991.tb00317.x.

55 Che X., Qiao W., Liu P., Ju X., Lu J. (2015) Identification of fractures in carbonates using sonic imaging log: Example from the central of East European Plain, *J. Acoustic. Soc. Am.* **137**, 2403–2404. https://doi.org/10.1121/1.4920754.

56 Crampin S. (2001) Shear-wave anisotropy: a new window into the crack-critical rockmass, *CSEG Record.* **26**, 07. https://csegrecorder.com/articles/view/shear-wave-anisotropy-a-new-window-into-the-crack-critical-rockmass.

José Perrin: ESEM-Polytech Orléans 1981 engineer, Geophysicist in BRGM/French Geological Survey: 1983–2019, Applied Geophysics for mineral exploration, hydrogeology and geotechnics, Borehole Geophysics in scientific drill holes, Airborne geophysics for Geological mapping, assignments in France, French Overseas territories, Africa, Middle East... Retired since 2019. https://www.researchgate.net/profile/Jose-Perrin/research.

Didier Belaud: ESPCI & ENSPM engineer, Geophysicist in IFP: 1978–1984, Geoscientist, acoustic domain champion in *Schlumberger*: 1984-2015, assignments in France, West Africa, Italy, Texas, Scotland, Venezuela, Abu Dhabi. Retired since 2015 https://www.linkedin.com/in/didier-belaud-72750826/?originalSubdomain=fr.

Jean-Pierre Yver: Polytechnique-Paris Engineer 1961, Field Engineer 1964–1979 then Petrophysicist in *Schlumberger*, up to 1997: assignments in Australia, Middle East, Africa, North Sea and France. Retired since 1997.

Charles Naville: Polytechnique-Paris 1973 & ENSPM Engineer, Geophysicist in *CGG* 1977–1989, field assignments in Gabon, USSR, USA, France, Geophysicist in IFPEN-France, 1990-present. https://www.researchgate.net/profile/Charles-Naville.